

MELT INFILTRATION OF CERAMIC PREFORMS FOR FUNCTIONALLY  
GRADED MATERIALS

A THESIS SUBMITTED TO  
THE GRADUATE SCHOOL OF NATURAL AND APPLIED SCIENCES  
OF  
MIDDLE EAST TECHNICAL UNIVERSITY

BY

CANER ERDAMAR

IN PARTIAL FULFILLMENT OF THE REQUIREMENTS  
FOR  
THE DEGREE OF MASTER OF SCIENCE  
IN  
METALLURGICAL AND MATERIALS ENGINEERING

DECEMBER 2019



Approval of the thesis:

**MELT INFILTRATION OF CERAMIC PREFORMS FOR FUNCTIONALLY  
GRADED MATERIALS**

submitted by **CANER ERDAMAR** in partial fulfillment of the requirements for the degree of **Master of Science in Metallurgical and Materials Engineering Department, Middle East Technical University** by,

Prof. Dr. Halil Kalıpçılar  
Dean, Graduate School of **Natural and Applied Sciences**

\_\_\_\_\_

Prof. Dr. C. Hakan Gür  
Head of Department, **Met. and Mat. Eng.**

\_\_\_\_\_

Prof. Dr. Ali Kalkanlı  
Supervisor, **Met. and Mat. Eng., METU**

\_\_\_\_\_

**Examining Committee Members:**

Prof. Dr. C. Hakan Gür  
Met. and Mat. Eng. / METU

\_\_\_\_\_

Prof. Dr. Ali Kalkanlı  
Met. and Mat. Eng., METU

\_\_\_\_\_

Prof. Dr. Arcan Fehmi Dericioğlu  
Met. and Mat. Eng. / METU

\_\_\_\_\_

Assist. Prof. Dr. Bilge İmer  
Met. and Mat. Eng. / METU

\_\_\_\_\_

Assist. Prof. Dr. Ayşe Kalemtaş  
Met. and Mat. Eng. / Bursa Teknik Üniversitesi

\_\_\_\_\_

Date: 09.12.2019

**I hereby declare that all information in this document has been obtained and presented in accordance with academic rules and ethical conduct. I also declare that, as required by these rules and conduct, I have fully cited and referenced all material and results that are not original to this work.**

Name, Surname: Caner Erdamar

Signature:

## ABSTRACT

### MELT INFILTRATION OF CERAMIC PREFORMS FOR FUNCTIONALLY GRADED MATERIALS

Erdamar, Caner  
Master of Science, Metallurgical and Materials Engineering  
Supervisor: Prof. Dr. Ali Kalkanlı

December 2019, 88 pages

The aim of this work was to produce ceramic-metal composite which shows combination of high hardness and high flexural strength by a combination of hard front layer and tough back layer by Functionally Graded Materials (FGM) process. Composition is the most important variable to obtain gradual changing green/bulk density and/or porosity which are the requirements of an FGM sample. Three different layers of FGM with gradual changing green density and/or porosity were pressed following by ball milling of different weight % of boron carbide and silicon carbide particles with different particle sizes. Each green body was sintered, and then, pressure melt infiltration process was applied to fill porosities with aluminum alloy in order to reach the near theoretical density. Finally, the material was characterized by phase analysis, particle size and distribution analysis, green/bulk density and porosity measurements, optical microscope and SEM analyses, three point bending test, hardness measurement and XRD analysis. Flexural strength measured for FGM B<sub>4</sub>C-SiC-Al composites having dimensions of 12 cm length, 4 cm width, 2.3 cm thickness is nearly  $348 \pm 40$  MPa.

Keywords: Functionally Graded Materials, Ceramic-Metal Composite, B<sub>4</sub>C-SiC-Al Composite, Melt Infiltration

## ÖZ

### FONKSİYONEL DERECELİ MALZEMELER İÇİN ÖN ŞEKİLLENDİRİLMİŞ SERAMİKLERİN İNFİLTRASYONU

Erdamar, Caner  
Yüksek Lisans, Metalurji ve Malzeme Mühendisliği  
Tez Danışmanı: Prof. Dr. Ali Kalkanlı

Aralık 2019, 88 sayfa

Bu çalışmanın amacı; ön sert tabaka ve arka sünek tabakanın birleşimiyle yüksek sertlik ve yüksek eğme dayanımı özelliği gösteren seramik-metal kompozitlerin Fonksiyonel Dereceli Malzeme (FDM) süreci ile üretilmesidir. FDM numunesinin gereksinimlerinden olan dereceli değişen yaş/yığınsal yoğunluk ve/veya porozite elde edilebilmesi için kompozisyon en önemli değişkenlerdendir. Farklı tane boyutlarına sahip bor karbür ve silisyum karbür tozlarının farklı ağırlık yüzdelerinde bilyalı değirmende öğütülmesi ve daha sonra preslenmesi ile dereceli değişen yaş yoğunluklara ve poroziteye sahip olan FDM'nin üç farklı tabakası üretildi. Üretilen her bir numuneye ısıtma işlemi uygulandı ve azami teorik yoğunluğa ulaşabilmek için basınçlı infiltrasyon süreciyle poroziteler alüminyum alaşımı ile dolduruldu. Son olarak; faz analizi, tane boyut ve dağılım analizi, yaş/yığınsal yoğunluk ve porozite ölçümü, optik mikroskop ve SEM analizi, üç nokta eğme testi, sertlik ölçümü ve XRD analizi ile kompozit malzemelerin karakterizasyonu gerçekleştirildi. 12 cm uzunluk, 4 cm genişlik ve 2,3 cm kalınlığa sahip FDM B<sub>4</sub>C-SiC-Al kompozitlerinin eğme dayanımı yaklaşık olarak 348 ± 40 MPa ölçüldü.

Anahtar Kelimeler: Dereceli Deęişen Malzemeler, Seramik-Metal Kompozit, Bor Karbür-Silisyum Karbür–Alüminyum Kompozit, İnfiltrasyon

To My Dear Family

## ACKNOWLEDGEMENTS

This study could not have been successfully conducted without the help and support of some people around me, to only some of whom it is possible to give particular mention here.

First of all, I would like to express my deepest gratitude to my supervisor Prof. Dr. Ali KALKANLI for his caring, support and guidance. I am really appreciated that he allowed me to use all the opportunities of his laboratory. It was a great honor to work with him and benefit from his knowledge and experiences.

Secondly, I would like to express my sincere appreciation to the technical staff of the Metallurgical and Materials Engineering Department of METU, Yusuf YILDIRIM, Cemal YANARDAĞ, Önder ŞAHİN and especially Ali Osman ATİK.

I also would like to present my sincere thanks to my friend who always answered my questions without tiredness and spared time to support my study, Cemre Metin POYRAZ.

Finally, the sincerest thanks to each of my family members Murat ERDAMAR, Ömer ERDAMAR and Aysel ERDAMAR for their support, encouragement, faith and love.

## TABLE OF CONTENTS

ABSTRACT .....	v
ÖZ.....	vi
ACKNOWLEDGEMENTS.....	ix
TABLE OF CONTENTS .....	x
LIST OF TABLES.....	xii
LIST OF FIGURES .....	xiii
LIST OF EQUATIONS .....	xvi
1. INTRODUCTION.....	1
2. LITERATURE REVIEW .....	3
2.1. THE CONCEPT OF FGM.....	3
2.2. THE FIRST APPLICATION OF FGM .....	7
2.3. DEFENCE APPLICATION OF FGM.....	7
2.4. B <sub>4</sub> C – SiC – Al <sub>2</sub> O <sub>3</sub> – Al COMPOSITES.....	10
2.5. MELT INFILTRATION .....	15
2.5.1. Pressureless Melt Infiltration.....	17
2.5.2. Pressure Melt Infiltration.....	21
3. AIM OF THE STUDY .....	25
3.1. MOTIVATION OF THE STUDY .....	25
3.2. MAIN CONTRIBUTION TO THE LITERATURE .....	26
4. EXPERIMENTAL PROCEDURE.....	27
4.1. PRODUCTION OF FGM LAYERS.....	28
4.2. PRODUCTION OF FGM .....	34

4.3. CHARACTERIZATION OF COMPOSITES.....	34
5. RESULTS AND DISCUSSION.....	41
5.1. PHASE ANALYSES .....	41
5.2. PARTICLE SIZE AND DISTRIBUTION ANALYSIS .....	43
5.3. GREEN DENSITY AND BULK DENSITY / POROSITY MEASUREMENTS .....	47
5.4. OPTIC EMISSION SPECTROMETER ANALYSIS.....	50
5.5. XRD ANALYSIS.....	50
5.6. OPTICAL MICROSCOPY ANALYSIS .....	55
5.7. SEM-EDX ANALYSIS .....	59
5.8. HARDNESS MEASUREMENTS .....	65
5.9. THREE POINT BEND TEST .....	65
6. CONCLUSIONS .....	69
6.1. CONCLUSIONS .....	69
6.2. RECOMMENDATIONS FOR FUTURE STUDY.....	71
REFERENCES.....	73
APPENDIX.....	79

## LIST OF TABLES

### TABLES

<b>Table 2.1.</b> NIJ Standard 0101.04 [9] .....	8
<b>Table 2.2.</b> Material properties and their roles in ballistic performance [3,10] .....	9
<b>Table 2.3.</b> Some properties of B <sub>4</sub> C, SiC, Al <sub>2</sub> O <sub>3</sub> and Al [16] .....	14
<b>Table 2.4.</b> Limit conditions of infiltration [15] .....	19
<b>Table 4.1.</b> The Layers of FGM .....	28
<b>Table 4.2.</b> The Layers of FGM .....	31
<b>Table 5.1.</b> Specific surface area of compositions .....	46
<b>Table 5.2.</b> Green densities of each composition .....	48
<b>Table 5.3.</b> Porosity % values of each composition .....	49
<b>Table 5.4.</b> Optic emission spectrometer analysis results of 7075 Al alloy and new composition which was modified from 7075 Al alloy for this study .....	50
<b>Table 5.5.</b> Phase analysis of FGM's layers which are (a) 90S10B, (b) 80S20B, (c) 70S30B as vol. % .....	58
<b>Table 5.6.</b> Aspect Ratio of B <sub>4</sub> C and SiC powders .....	61
<b>Table 5.7.</b> Hardness measurements of Al alloy infiltrated 90S10B, 80S20B and 70S30B composites .....	65
<b>Table 5.8.</b> Three point bend test results .....	66

## LIST OF FIGURES

### FIGURES

<b>Figure 2.1.</b> The schematic view of the FGM structure [5] .....	4
<b>Figure 2.2.</b> The differences in structure and properties between FGM and conventional composite materials [7] .....	5
<b>Figure 2.3.</b> (a) Some problems due to joining of ceramic and metal, (b) The role of gradient for interlayer [2] .....	6
<b>Figure 2.4.</b> Projectile – Armor interaction in FGM [1] .....	10
<b>Figure 2.5.</b> Image of CES Edupack program that shows density and hardness of ceramic materials .....	11
<b>Figure 2.6.</b> Image of CES Edupack program that shows price and thermal expansion coefficient of ceramic materials .....	12
<b>Figure 2.7.</b> The phase diagram of the B <sub>4</sub> C – SiC system [17] .....	13
<b>Figure 2.8.</b> Illustration of the wetting and non-wetting conditions between solid ceramic and liquid metal [22] .....	16
<b>Figure 2.9.</b> Illustration of the pressureless melt infiltration [29] .....	17
<b>Figure 2.10.</b> Green density vs B <sub>4</sub> C content [15] .....	19
<b>Figure 2.11.</b> The infiltration mechanism of B <sub>4</sub> C – SiC - Al composite [15] .....	20
<b>Figure 2.12.</b> Illustration of the pressure melt infiltration [26] .....	21
<b>Figure 3.1.</b> Expected structure and mechanical properties.....	25
<b>Figure 4.1.</b> Experimental flow chart.....	27
<b>Figure 4.2.</b> Ball milling machine and jar filled with ingredients .....	29
<b>Figure 4.3.</b> Pressing operation and green ceramic body .....	30
<b>Figure 4.4.</b> Furnace and temperature vs time graph of the sintering process.....	31
<b>Figure 4.5.</b> Pressure melt infiltration process.....	32
<b>Figure 4.6.</b> Preparation of new Al alloy .....	33

<b>Figure 4.7.</b> Preheated die and 90S10B composite after aluminum pressure melt infiltration process .....	33
<b>Figure 4.8.</b> (a) Specimen geometry, (b) Normal stress variation, (c) Shear stress variation, (d) Normal strain variation [31] .....	39
<b>Figure 5.1.</b> Ternary phase diagram of B, C and Si elements at 1400 °C .....	42
<b>Figure 5.2.</b> Calculation of mass percent of elements in 90S10B composition .....	42
<b>Figure 5.3.</b> Ternary phase diagram of Al, Mg and Si elements at 700 °C .....	43
<b>Figure 5.4.</b> Particle size and distribution analysis of 90S10B .....	45
<b>Figure 5.5.</b> Particle size and distribution analysis of 80S20B .....	45
<b>Figure 5.6.</b> Particle size and distribution analysis of 70S30B .....	45
<b>Figure 5.7.</b> Variation of d(0.5) values with respect to B <sub>4</sub> C content.....	46
<b>Figure 5.8.</b> Variation of specific surface area values with respect to B <sub>4</sub> C content...	47
<b>Figure 5.9.</b> Green density variation with B <sub>4</sub> C content .....	48
<b>Figure 5.10.</b> Porosity % variation with B <sub>4</sub> C content.....	49
<b>Figure 5.11.</b> XRD analysis of sintered 80S10B10A .....	51
<b>Figure 5.12.</b> 80S10B10A sample was put into water and crashed .....	52
<b>Figure 5.13.</b> XRD analysis of Al alloy .....	53
<b>Figure 5.14.</b> XRD analysis of Al alloy infiltrated 70S30B composite .....	53
<b>Figure 5.15.</b> XRD analysis of Al alloy infiltrated 80S20B composite .....	54
<b>Figure 5.16.</b> XRD analysis of Al alloy infiltrated 90S10B composite .....	54
<b>Figure 5.17.</b> XRD analysis of Al alloy infiltrated FGM .....	55
<b>Figure 5.18.</b> The microstructure of Al alloy .....	56
<b>Figure 5.19.</b> Microstructure of FGM .....	57
<b>Figure 5.20.</b> Phase analysis of FGM's layers which are (a) 90S10B, (b) 80S20B, (c) 70S30B .....	57
<b>Figure 5.21.</b> Phase analyses of Al alloy infiltrated (a) 90S10B, (b) 80S20B and (c)70S30B layers .....	58
<b>Figure 5.22.</b> SEM analysis of B <sub>4</sub> C powder .....	60
<b>Figure 5.23.</b> SEM analysis of SiC powder.....	60

<b>Figure 5.24.</b> SEM-EDX analysis of SiC region of Al infiltrated 80S20B composite .....	62
<b>Figure 5.25.</b> SEM-EDX analysis of Al alloy / B <sub>4</sub> C region of Al alloy infiltrated 80S20B composite .....	63
<b>Figure 5.26.</b> SEM-EDX analysis of Mg <sub>2</sub> Si region of Al alloy infiltrated 80S20B composite .....	64
<b>Figure 5.27.</b> Flexural strength with respect to B <sub>4</sub> C content .....	66
<b>Figure 5.28.</b> FGM with Al alloy base specimen subjected to three point bend test..	67
<b>Figure 6.1.</b> Armor design for future study .....	71
<b>Figure A.1.</b> Flexure load-Flexure extension graph of Al alloy specimen 1 .....	79
<b>Figure A.2.</b> Flexure load-Flexure extension graph of Al alloy specimen 2 .....	80
<b>Figure A.3.</b> Flexure load-Flexure extension graph of FGM specimen 1 .....	81
<b>Figure A.4.</b> Flexure load-Flexure extension graph of FGM specimen 2 .....	82
<b>Figure A.5.</b> Flexure load-Flexure extension graph of Al alloy infiltrated 70S30B specimen 1 .....	83
<b>Figure A.6.</b> Flexure load-Flexure extension graph of Al alloy infiltrated 70S30B specimen 2 .....	84
<b>Figure A.7.</b> Flexure load-Flexure extension graph of Al alloy infiltrated 80S20B specimen 1 .....	85
<b>Figure A.8.</b> Flexure load-Flexure extension graph of Al alloy infiltrated 80S20B specimen 2 .....	86
<b>Figure A.9.</b> Flexure load-Flexure extension graph of Al alloy infiltrated 90S10B specimen 1 .....	87
<b>Figure A.10.</b> Flexure load-Flexure extension graph of Al alloy infiltrated 90S10B specimen 2 .....	88

## LIST OF EQUATIONS

### EQUATIONS

<b>Equation 4.1.</b> Green density calculation for manual pressed green ceramic bodies	35
<b>Equation 4.2.</b> Green density calculation for double action pressed green ceramic bodies.....	35
<b>Equation 4.3.</b> Calculation of bulk density and porosity % by using xylene solution .....	36
<b>Equation 4.4.</b> Calculation of bulk density and porosity % by using distilled water	37
<b>Equation 4.5.</b> (a) Calculation of flexural strength, (b) Calculation of flexural strength when $c = h/2$ .....	38
<b>Equation 5.1.</b> $Al_4C_3$ and $Al(OH)_3$ formation reactions .....	51

## CHAPTER 1

### INTRODUCTION

In defense applications, the development of armor materials with low density, high hardness and high flexural strength is very important to obtain weight materials with improved performance properties such as wear resistance and energy absorption. Three main material classes which are ceramics, metals and composites are preferred for ballistic threats. Engineering ceramics have superior properties such as high elastic modulus, high wear and corrosion resistance, low density and low thermal expansion coefficient. However, they have poor fracture toughness and high expense which limits their industrial applications. Metals are strong, ductile, good thermal and electrical conductor. However, they are not well suited for high temperature applications, shrink or expand with temperature changes and are prone to chemical and corrosion attacks. Composite materials are advance materials consist of one or more materials with distinct properties. They exhibit the best of properties of combinations which are different from individual materials. Achieving the best properties with eliminating undesirable ones led to come up with a new class of material called FGM which is the shortening of “Functionally Graded Materials”. FGM can be considered as an effective armor material because it serves different actions at different layers [1, 2, 3].

In this thesis,  $B_4C - SiC - Al$  composites that have low density and a combination of high hardness and flexural strength were produced by cost effective melt infiltration process to obtain FGM which may be used against ballistic threats. Also, the production of high ceramic fraction composites with minimized porosity at lower temperatures ( $<1400\text{ }^\circ\text{C}$ ) was aimed. The specimens were characterized by phase analysis, green/bulk density and porosity measurements, particle size and distribution

analysis, X-ray diffraction (XRD) analysis, light microscope and scanning electron microscope (SEM) analyses, hardness measurement and three point bending test.

## CHAPTER 2

### LITERATURE REVIEW

#### 2.1. THE CONCEPT OF FGM

Achieving the best properties with eliminating undesirable ones led to come up with a new class of material called FGM which is the shortening of “Functionally Graded Materials”. Due to their unique properties, FGM have attracted great attention from researchers in many fields such as future space programs, biomaterials, armor materials. FGM have a continuous variation of material properties like thermal, mechanical and electrical properties with respect to position due to non-homogeneous microstructure, atomic order or chemical composition. With the FGM concept, specific materials for specific applications can be produced. Some applications of FGM are as follows: smart structures, MEMs and sensors, electronics and optoelectronics, medicine, biomaterials, power plant, manufacturing, aerospace and aeronautics, energy, defense [4].

Powder metallurgy process with two or more powders may be used to obtain FGM with a stepwise structure. The schematic view of the FGM structure is illustrated in Figure 2.1. There are phase changes from the upper part to the lower part as the volume fraction of B phase increases. Both A and B phases may serve as a matrix. The upper part consists of phase-B particles embedded in Phase-A matrix called A dominant part. Whereas, the lower part consists of phase-A particles embedded in phase-B matrix called B dominant zone. There is a transition zone in the middle part because the dominant phase can't be determined easily.

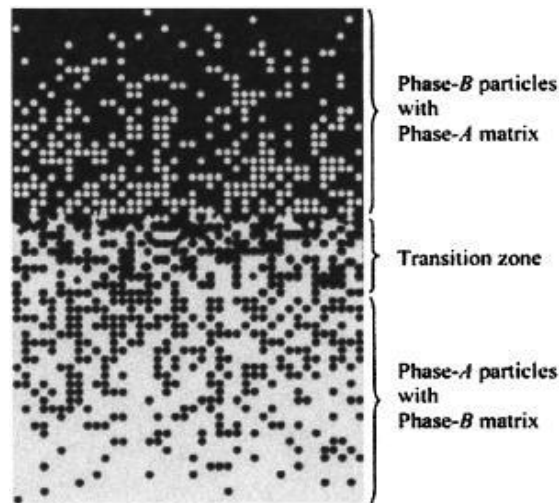


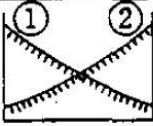
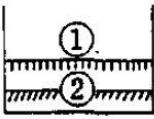
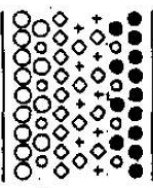
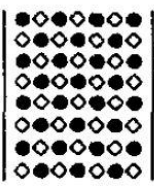
**Figure 2.1.** The schematic view of the FGM structure [5]

The manufacturing process of FGM is categorized into two groups which are gradation and consolidation. Gradation is the forming of an inhomogeneous structure. Consolidation is the conversion of this inhomogeneous structure into the bulk material. Gradation processes can be divided into constitutive, homogenizing and segregating processes. The constitutive process is based on stepwise forming of the graded structure from powders. In the homogenizing process, a sharp interface between two materials is transformed into a gradient by material transport. Segregating processes start with a macroscopically homogeneous material that is transformed into a graded material by material transport resulted from an external field [4].

Gradation provides the material to have desirable properties of each component at a specific layer. For instance, ceramic-metal FGM have properties of metal such as high fracture toughness and high electrical and thermal conductivity without eliminating required properties of ceramic such as high hardness and high thermal resistance. Gradation can be supplied by gradual changing of microstructure, atomic order or chemical composition from one end to the other [5]. Ceramic-metal FGM may be obtained by building-up a ceramic preform with graded porosity (green density) and

its melt infiltration with molten metal. A graded preform is built up layer by layer with each layer containing an appropriate amount of constituent powders. Layers are compacted and/or sintered into a bulk form that exhibits variation of porosity. According to porosity content, the required amount of metal to fill all pores is calculated then infiltrated in appropriate conditions. The resulting material exhibits a differing ceramic-metal ratio and so properties [6].

The differences in structure and properties between FGM and non-FGM (conventional composite materials) are illustrated in Figure 2.2. For non-FGM, ceramic and metal phases are distributed homogeneously so thermal conductivity and mechanical strength don't change with position. While for FGM, ceramic and metal phases are distributed non-homogeneously so thermal conductivity and mechanical strength change with position. Because the left part mostly consists of ceramic phases, mechanical strength is higher and thermal conductivity is lower. Because the right part mostly consists of metal phases, thermal conductivity is higher and mechanical strength is lower.

<b>Function/ Property</b>	① Mechanical Strength ② Thermal Conductivity		
<b>Structure/ Texture</b>	<b>Constituent Elements:</b> Ceramics (○) Metal (●) Fiber (◇+) Micropore (○)		
<b>Materials</b>	<b>Example</b>	<b>FGM</b>	<b>non-FGM</b>

**Figure 2.2.** The differences in structure and properties between FGM and conventional composite materials [7]

The joining of dissimilar materials is so difficult and problematic. Because different materials have different thermal expansion coefficient, the combination of them results in residual stress due to ceramics do not undergo plastic deformation to accommodate volume changes. Also, different volumes of different materials cause undesirable reactions at the interface. To cope with these problems, FGM as interlayers has been established. FGM annihilates the sharp interfaces in composite materials in which failure is initiated. It transforms this sharp interface to a gradient interface and a smooth transition from one material to others is obtained. Some problems due to the joining of ceramic and metal and the role of gradient for interlayer are illustrated in Figure 2.3. Inclusions, unjoined islands or pores, reaction layer with cracks, surface damage, unjoined edge, interface flaw and crack into ceramic may form between ceramic and metal without gradient. When the interlayer has no gradient (top), the pieces do not join. However, when a graded interlayer is used (bottom), the two pieces can be successfully joined to each other.

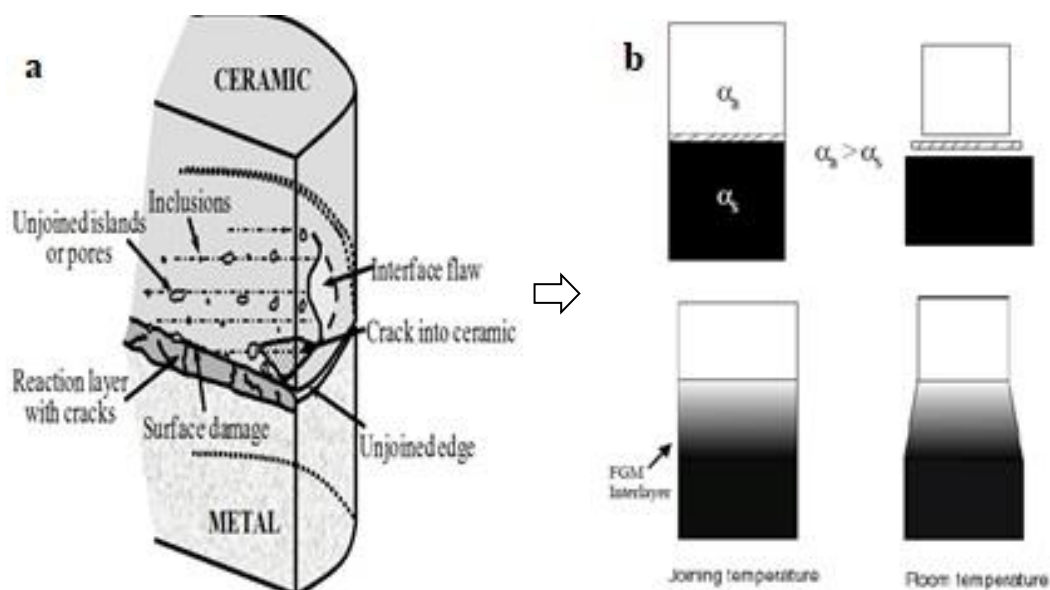


**Figure 2.3.** (a) Some problems due to joining of ceramic and metal, (b) The role of gradient for interlayer [2]

## **2.2. THE FIRST APPLICATION OF FGM**

FGM concept has arisen in 1984 by material scientists in Japan for the spacecraft industry. The outer surface of the spacecraft should be durable against high temperature and high temperature changes. At that time there was no suitable material that could resist this high thermomechanical loading. Thus, Dr. Niino et al. prepared a thermal barrier material that was a new composite by using heat resistant ceramic at high temperature zone and high thermal conductive metal at low temperature zone with gradual changing of ceramic/metal composition. By this way, the outer surface of the spacecraft was protected by gradual distribution of temperature [7].

## **2.3. DEFENCE APPLICATION OF FGM**

The development of armor materials that have low density and high protection ability is very crucial for defense applications. There are a lot of parameters that should be considered for choosing materials in armor system. In ballistic attacks, the most widely used threat type is the projectile with various calibers, core hardness and velocity. Therefore, the ballistic resistance of armor against these kinds of projectiles should be considered. Personnel armor can be classified into soft armor (textile based systems with fibers) and hard armor (ceramic, metal or ceramic-metal composite). Soft armors are used against low level threats (NIJ level III or less), whereas hard armors are used against higher level threats (NIJ level IV) Hence, there is no single best armor material against all threats which are given in Table 2.1 [8].

**Table 2.1.** NIJ Standard 0101.04 [9]

Armor Type	Test Round	Test Bullet	Bullet Weight	Reference Velocity ( $\pm 30$ ft/s)	Hits Per Armor Part at 0° Angle of Incidence	BFS Depth Maximum	Hits Per Armor Part at 30° Angle of Incidence	Shots Per Panel	Shots Per Sample	Shots Per Threat	Total Shots Req'd
I	1	.22 caliber LR LRN	2.6 g 40 gr.	329 m/s (1080 ft/s)	4	44 mm (1.73 in)	2	6	12	24	48
	2	.380 ACP FMJ RN	6.2 g 95 gr.	322 m/s (1055 ft/s)	4	44mm (1.73 in)	2	6	12	24	
IIA	1	9 mm FMJ RN	8.0 g 124 gr.	341 m/s (1120 ft/s)	4	44 mm (1.73 in)	2	6	12	24	48
	2	40 S&W FMJ	11.7 g 180 gr.	322 m/s (1055 ft/s)	4	44 mm (1.73 in)	2	6	12	24	
II	1	9 mm FMJ RN	8.0 g 124 gr.	367 m/s (1205 ft/s)	4	44 mm (1.73 in)	2	6	12	24	48
	2	357 Mag JSP	10.2 g 158 gr.	436 m/s (1430 ft/s)	4	44 mm (1.73 in)	2	6	12	24	
IIIA	1	9 mm FMJ RN	8.2 g 124 gr.	436 m/s (1430 ft/s)	4	44 mm (1.73 in)	2	6	12	24	48
	2	44 Mag JHP	15.6 g 240 gr.	436 m/s (1430 ft/s)	4	44 mm (1.73 in)	2	6	12	24	
III	1	7.62 mm NATO FMJ	9.6 g 148 gr.	838 m/s (2780 ft/s)	6	44 mm (1.73 in)	0	6	12	12	12
IV	1	.30 caliber M2 AP	10.8 g 166 gr.	869 m/s (2880 ft/s)	1	44 mm (1.73 in)	0	1	2	2	2
Special	*	*	*	*	*	44 mm (1.73 in)	*	*	*	*	*

Panel = Front or back component of typical armor sample.  
 Sample = Full armor garment, including all component panels (F & B).  
 Threat = Test ammunition round by caliber.

Some important properties that affect ballistic properties are required for armor systems as shown in Table 2.2. Firstly, the weight of the armor system is based on density so materials that have low density should be used to enhance maneuver capacity. Only materials that have higher hardness value of that of the projectile can break up the projectile when it strikes on the armor system. The ballistic performance of the armor system depends on also compressive and tensile strength. Compressive strength is related with the thickness of the armor system for protection. Materials that have low tensile strength fail at an early stage of the perforation process without exhibiting high compressive strength. Hence, high strength provides multi-hit resistance.

**Table 2.2.** Material properties and their roles in ballistic performance [3,10]

Property	Role / Effect in ballistic performance
Microstructure Grain Size Minor phases Phase transformation or Amorphization Porosity	Affects all properties listed in the left-hand column below
Density	Weight of the armor system
Hardness	Damage to the projectile
Strength	Multi hit resistance

In ballistic attacks, projectile should be stopped without harming threat. The time which projectile is kept at the ceramic surface prior to penetration is described as dwell. A cone that spreads out below the projectile is formed at damaged material. This causes spreading of load of the impact over larger areas of the backing material, thus stress reduces. Backing material should exhibit high flexural strength to not allow penetration so it stops the projectile. Backface deformation should be limited to not to harm threat. Hence, the ratio of dwell, erosion and backing deformation is determined by the armor system and the threat [30].

Functionally Gradient Material (FGM) can be considered as an effective armor material because it serves different actions at different layers. A combination of the hard outer layer consists of mostly ceramic phases and the tough inner layer consists of mostly metal phases provides effective protection against ballistic threats. Projectile – armor interaction in FGM is illustrated in Figure 2.4. The outer hard layer of FGM shatters the projectile whereas the inner tough layer of FGM stops the projectile and shrapnel via absorbing its kinetic energy.

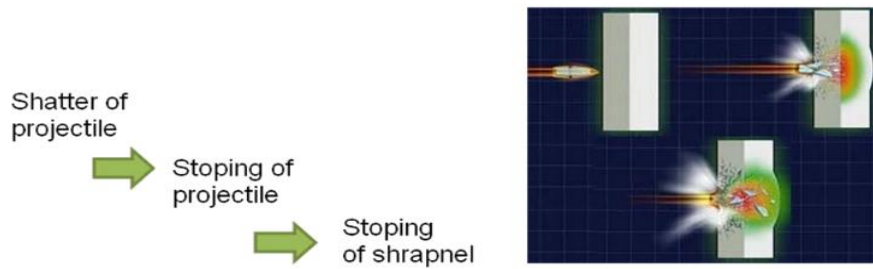


**Figure 2.4.** Projectile – Armor interaction in FGM [1]

## 2.4. $B_4C$ – $SiC$ – $Al_2O_3$ – $Al$ COMPOSITES

To provide maximum protection against high level ballistic threats, a new type of material consisting of different layers that serve different actions must be developed. The use of high volume fraction ceramic materials for front plate and high volume fraction metal materials for backing plate in the form of FGM has been considered to replace with non-FGM in armor technologies [11].

Increasing the thickness of steel and Al armor materials to provide maximum protection against high ballistic threats is not acceptable because it increases the weight of the armor system. Thus, ceramic based armors that have low density and extreme ballistic performance may be considered as a good solution [10]. The most common ceramics used for armor applications are aluminum oxide (alumina), silicon carbide and boron carbide. Alumina is the most economical choice, but it has higher density and less ballistic efficiency than boron carbide and silicon carbide. Boron carbide is the hardest ceramic and has very low density among them, but it is not effective alone against armor piercing projectiles with high impact velocity because of the weakening of ceramic by the amorphization process and it is very expensive. Boron carbide is a good option for one-hit protection. When multi-hit protection is needed, boron carbide can be used with silicon carbide which has close hardness that of  $B_4C$  and doesn't undergo amorphization process. The density of silicon carbide is

a bit higher than that of boron carbide, but the hardness of silicon carbide is very close to that of boron carbide and the price of silicon carbide is lower than that of boron carbide. Also, the thermal expansion coefficient value of silicon carbide is very close to that of boron carbide that minimizes residual stress formed because of different thermal expansion of different materials. Thus, it can be considered that silicon carbide is a very effective material for armor technologies. Pressure transmitted to the backside of the ceramic causes high tensile stresses that result in cracks propagating radially outwards on the backside of the ceramic tile.  $\text{Al}_2\text{O}_3$  ceramic is broken up into larger fragments which provide blocking of the penetrator. Hence it gives higher penetration and abrasion resistance to composite. The choice between these types of ceramic materials depends on which threat level, weight restrictions and price are dominant. Figure 2.5 and Figure 2.6 show some of the important parameters for armor materials [3].

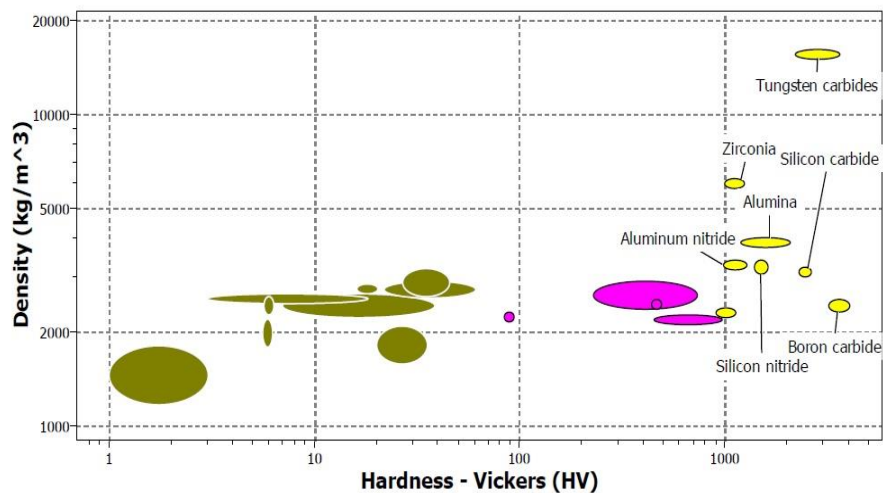


**Figure 2.5.** Image of CES Edupack program that shows density and hardness of ceramic materials

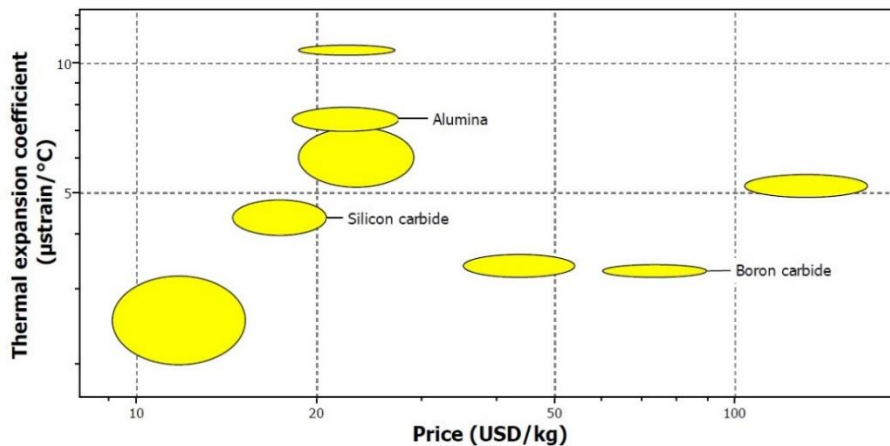


**Figure 2.6.** Image of CES Edupack program that shows price and thermal expansion coefficient of ceramic materials

Boron carbide is the hardest third material that can exhibit 30 GPa followed by diamond and cubic-BN. At temperatures higher than 1200 °C, the hardness of B<sub>4</sub>C may be higher than the hardness of diamond [12]. Since B<sub>4</sub>C has high hardness and low density, it is best as armor material. Nevertheless, industrial use of B<sub>4</sub>C is restricted due to its high cost, sintering difficulties, low toughness and machinability [13]. Also, B<sub>4</sub>C is not well suited against high speed armor piercing projectiles because of the amorphization process in B<sub>4</sub>C when it is exposed to high pressure in which protection capability of B<sub>4</sub>C decreases since shear strength of B<sub>4</sub>C decreases. Also, because B<sub>4</sub>C is very brittle, it does not provide efficient protection against shot more than one [3].

The use of silicon carbide in the armor system is very popular since price/performance ratio is getting better [14]. The availability of SiC is easier than that of B<sub>4</sub>C since the use of SiC is higher than the use of B<sub>4</sub>C in other sectors. SiC is cheaper than B<sub>4</sub>C and it behaves like B<sub>4</sub>C in armor system. Thus, the use of B<sub>4</sub>C is tried to keep low for this system by scientists work for this sector [15]. Even monolithic SiC can be used in the armor system, it can also be mixed with B<sub>4</sub>C. The density of SiC is 3.21 g/cm<sup>3</sup> which is a bit higher than the density of B<sub>4</sub>C and lower than the density of Al<sub>2</sub>O<sub>3</sub>. Also, the

hardness of SiC is so close to the hardness of B<sub>4</sub>C. Hence, even SiC has higher density than B<sub>4</sub>C, SiC can be considered as a good choice against high level ballistic threats such as NIJ IV [3]. Figure 2.7 illustrates the phase diagram of the B<sub>4</sub>C-SiC system. The presence of silicon carbide decreases the melting temperature of boron carbide to below 2250 °C. This result is supported by the observed eutectic reaction between B<sub>4</sub>C and SiC. Researchers have found different eutectic temperatures with different SiC addition.

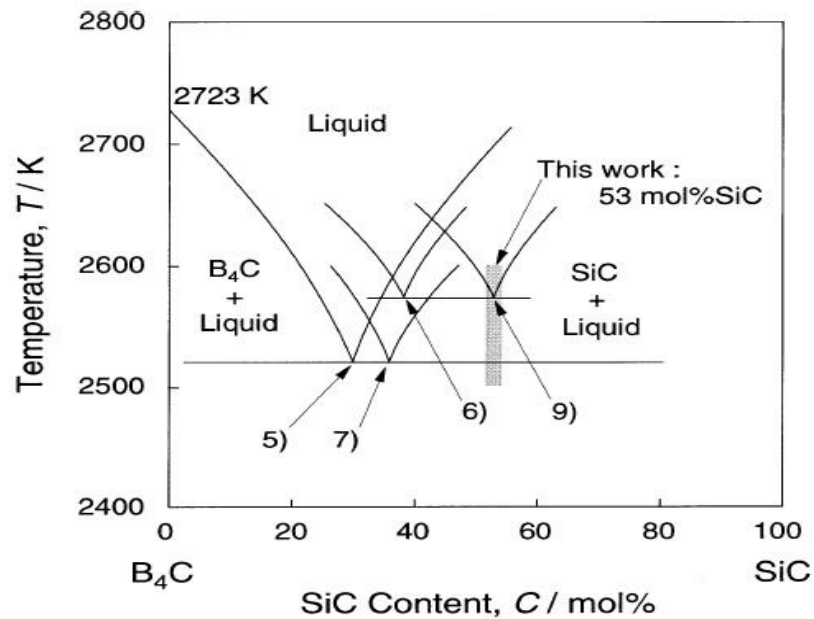


**Figure 2.7.** The phase diagram of the B<sub>4</sub>C – SiC system [17]

Solid state sintering of SiC can be achieved via sintering aids such as B<sub>4</sub>C as sources of B and C elements and glucose as source of C elements. B elements enable diffusion in SiC by increasing the energy of the structure. It causes to formation of stacking faults, so stress field to balance these. Also, B elements cause more grain growth during sintering. C elements enable direct contact between SiC particles by removing SiO<sub>2</sub> coating on SiC particles. Also, C elements cause lowering the temperature of the formation of Si-B-C liquid [30].

However ceramic armors are mostly used nowadays, the use of ceramic armors is restricted because of their poor fracture toughness and high cost. They do not exhibit enough protection against shots more than one in a short time. After first shot strikes to armor, armor is fractured and it allows to the penetration of following projectiles [18]. Armor system which includes a combination of ceramic and metal can exhibit better protection. Thus, the formation of the ceramic preform with porosities and infiltration of this ceramic preform with metal can solve this problem. Aluminum and its alloys are used for infiltration by many researchers due to their low density, low melting point and high ductility. They are also cheaper and available. Melted aluminum and its alloys can be easily infiltrated, thus materials with almost 0 % porosity can be developed. Produced ceramic-metal composites display both high hardness and high flexural strength with low density [19].

Table 2.3 shows some properties which are important for the armor system of B<sub>4</sub>C, SiC, Al<sub>2</sub>O<sub>3</sub> and Al.

**Table 2.3.** Some properties of B<sub>4</sub>C, SiC, Al<sub>2</sub>O<sub>3</sub> and Al [16]

<b>Materials</b>	<b>Density (g/cm<sup>3</sup>)</b>	<b>Melting Point (°C)</b>	<b>Hardness (Knoop)</b>	<b>Fracture Toughness (MPa.m<sup>-1/2</sup>)</b>
<b>B<sub>4</sub>C</b>	2.52	2445	2750	2.9 - 3.7
<b>SiC</b>	3.21	2730	2480	4.3
<b>Al<sub>2</sub>O<sub>3</sub></b>	4.00	2070	2100	3.3 – 5.0
<b>Al</b>	2.70	660	120	29

## 2.5. MELT INFILTRATION

Production of highly dense boron carbide – silicon carbide - alumina composites is so difficult because of hard covalent bonds, high endurance to grain boundary sliding, lack of plastic behavior which restrict their diffusion in sintering. In addition to the high price of powders, both high temperature and high pressure applied in sintering make this process very expensive [19]. In contrast to traditional sintering processes, the melt infiltration process is widely used to develop composite from ceramic preforms with porosities. Some advantages of the melt infiltration process are as follows. Near or near-net shape composites which include high vol. % ceramic can be produced. Also, the microstructure of composites may show a uniform distribution of ceramic phases [20]. The formation of residual stress because of different thermal expansion coefficient of different material may be prohibited, hence residual porosities may be eliminated. With the use of suitable materials, physical and mechanical properties of the composite may be adjusted [21]. By this process, the reaction rate between constituent materials and reaction products may be managed.

Wetting conditions between solid ceramic and liquid metal is very important for the melt infiltration process. Wettability is the capability of a liquid to cover the solid surface when liquid and solid get in touch [15]. The reduction of free energy of the system is the driving force for wetting. When there is no wetting, ceramic and metal do not react with each other. Thus, the wetting of the solid ceramic by liquid metal should be provided to achieve the infiltration process [22]. To do that, the suitable temperature and atmospheric situation should be selected. By this way, liquid metal is sucked into porosities in ceramic preform by capillarity thermodynamic criteria [21]. Figure 2.8 illustrates the wetting and non-wetting conditions between solid ceramic and reactive liquid metal. When the contact angle is lower than  $90^\circ$  wetting condition is obtained, whereas when the contact angle is higher than  $90^\circ$  non-wetting condition is obtained.

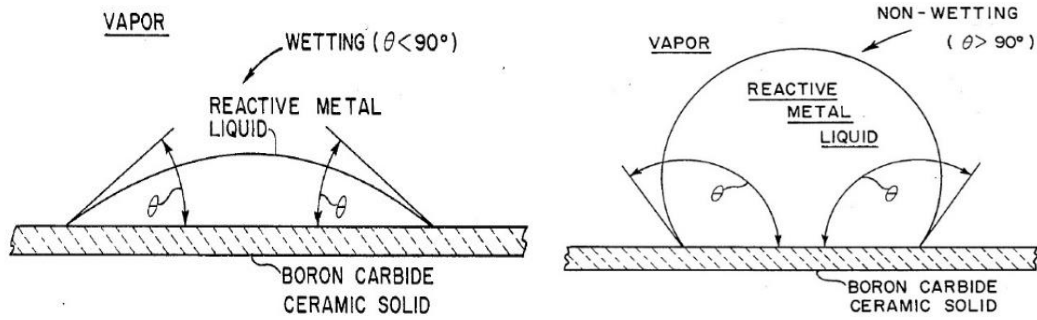


**Figure 2.8.** Illustration of the wetting and non-wetting conditions between solid ceramic and liquid metal [22]

Wettability of ceramics with liquid Al metals is generally poor due to the existence of contamination, humidity, oxide and gas layer which covers the solid ceramic powders surface and aluminum oxide layer that covers the liquid Al. Because of these obstacles, the melted metal may not get in touch with the solid ceramic powders surface. In order to enhance the wetting of solid ceramic powders by liquid metal, researchers have found some procedures: (i) increasing temperature of liquid metal, (ii) addition of alloying elements like Ca, Mg, Ti, Ca, Zr, Li, (iii) oxidizing or coating of ceramic particles, (iv) cleaning the particles. By this way surface energy of the ceramic particles increases and surface tension of the liquid metal decreases at the ceramic particle – liquid metal interface [15].

Melt infiltration process is very economical because exposure of the material to high temperature and high pressure is eliminated. If wettability is ensured, even exposure of the material to pressure is not necessary. Melt infiltration may be achieved via two ways: pressureless melt infiltration and pressure melt infiltration.

### 2.5.1. Pressureless Melt Infiltration

In pressureless melt infiltration, a solid metal block is placed top of a ceramic preform and compacted in a furnace in an inert atmosphere. Figure 9 shows the pressureless melt infiltration process.

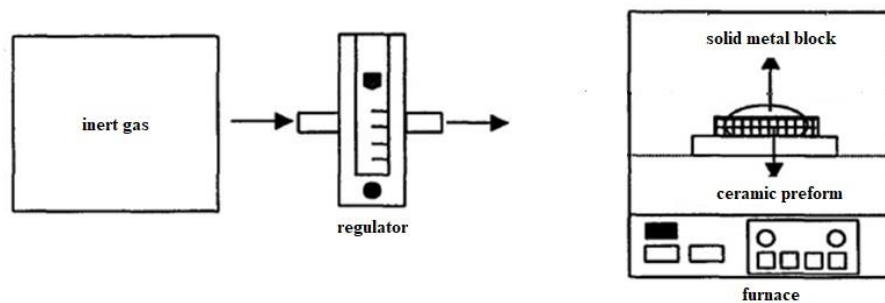


**Figure 2.9.** Illustration of the pressureless melt infiltration [29]

In this thesis, B<sub>4</sub>C-SiC ceramic preform was infiltrated with Al alloy.

B<sub>4</sub>C has more reactivity with Al in the excess of 500 °C. At temperature range between 900 – 1125 °C, the main reaction products are Al<sub>3</sub>BC and AlB<sub>2</sub>. At higher temperatures, Al<sub>3</sub>BC may be replaced by Al<sub>4</sub>C<sub>3</sub> which is a detrimental reaction product. Thus, the reaction rate between B<sub>4</sub>C and Al should be controlled. Otherwise, the metallic phase may be consumed before complete infiltration that results in considerable porosity in the composite and the reaction layer may form which may inhibit further infiltration of liquid metal [24]. This situation may cause the failure of the infiltration process due to the earlier formation of reaction products which may lock microstructure. Pyzik et al have worked to decrease the reactivity of B<sub>4</sub>C with Al by passivating B<sub>4</sub>C particles prior to infiltration process. Passivation provides controlling of the kinetics of molten metal infiltration and rate of formation of reaction products. Reaction products like AlB<sub>2</sub>, Al<sub>4</sub>BC, AlB<sub>12</sub>C<sub>2</sub>, AlB<sub>12</sub> and Al<sub>4</sub>C<sub>3</sub> affect

negatively some mechanical properties of the composite. For example,  $Al_4BC$  is a detrimental phase because it is more brittle than  $B_4C$  and Al. Lower reactivity provided by the passivation process decreases the formation of undesirable ceramic phases. There are two different forms of surface boron ( $B_3$  and  $B_3'$ ) in ceramic preforms that are passivated in the temperature range of 1250 – 1400 °C.  $B_3'$  is more reactive than  $B_3$ .  $B_3'$  content is zero or near zero when the passivation process is applied at temperatures higher than 1400 °C. All the surface borons are in the form of  $B_3$ . Infiltration of preform takes place much faster at lower temperatures in the presence of the passivation process prior to sintering. For example, passivation at 1400 °C with 2 hours provides infiltration at lower than 1000 °C [25].

Arslan and Kalemtaş have worked to develop  $B_4C$  - SiC - Al composites which contain low  $B_4C$  contents by using cost effective pressureless melt infiltration method for impact applications.  $B_4C$  addition improves the wettability of SiC by Al. However, its high cost limits its industrial applications. Thus,  $B_4C$  content should be optimized to the minimum value as much as possible. Table 4 shows the required temperatures and times for different  $B_4C$  and SiC compositions for this process. When there is no  $B_4C$  in the composite, even at temperatures in the excess of 1400 °C with 60 minutes, only partial infiltration is achieved. When there is 5 wt. %  $B_4C$  in the composite, required temperature for full infiltration drops to 1130 °C. Nevertheless, at temperatures in the excess of 1050 °C, detrimental reaction product  $Al_4C_3$  is formed in significant amounts. When there is 10 wt. %  $B_4C$  in the composite, the required temperature for full infiltration decreases towards 985 °C and required time decreases to 30 minutes. Also, the amount of porosity is so low for composites that contain minimum 10 wt. %  $B_4C$ .

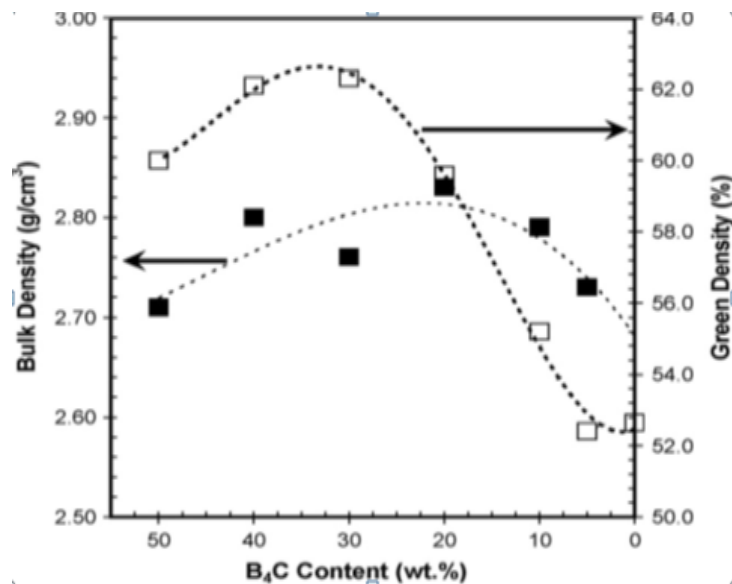
**Table 2.4.** Limit conditions of infiltration [15]

Chemical composition of prepared powder mixtures and limit conditions of infiltration

Composition	SiC (wt.%)	B <sub>4</sub> C (wt.%)	Temperature (°C)	Time (min)
50S50B	50	50	985	60
60S40B	60	40	1035	10
70S30B	70	30	1035	10
80S20B	80	20	935	60
90S10B	90	10	985	30
95S5B	95	5	1130	60
100S <sup>a</sup>	100	0	1420 <sup>a</sup>	60 <sup>a</sup>

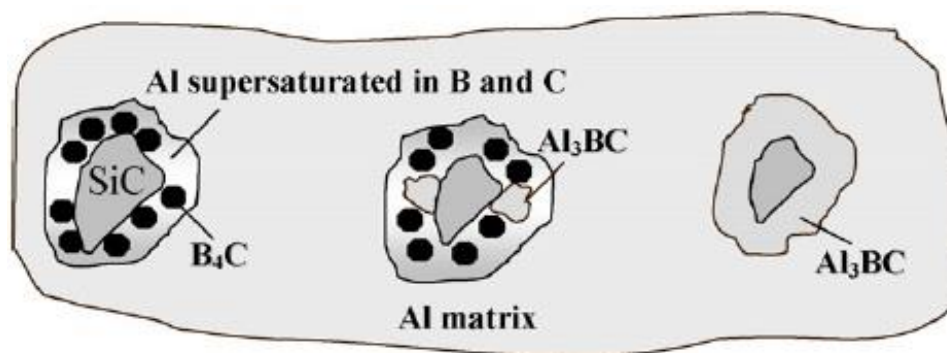
<sup>a</sup> Partial infiltration (~2.4 mm).

Figure 2.10 shows green density variation with respect to B<sub>4</sub>C content. The lowest green density is obtained with 0 wt. % B<sub>4</sub>C, the highest green density is obtained with 30 wt. % B<sub>4</sub>C. Green density decreases gradually from 30 wt. % to 10 wt. % B<sub>4</sub>C. But, further addition of B<sub>4</sub>C causes decreasing of green density. Hence, FGM design with 3 different layers containing 30 wt. %, 20 wt. % and 10 wt. % of B<sub>4</sub>C can be considered to provide different amounts of molten metal due to gradual changing of green density and by this way, gradual changing mechanical properties can be obtained.



**Figure 2.10.** Green density vs B<sub>4</sub>C content [15]

Figure 2.11 shows the infiltration mechanism of  $B_4C$  - SiC - Al composite. During the infiltration process,  $Al_3BC$  formation takes place due to interaction between  $B_4C$  and Al. Coarse SiC particles are confined with  $Al_3BC$  particles and suppress a significant amount of  $Al_4C_3$  formation. It is reported that 10 wt. % fine  $B_4C$  is enough to cover the surfaces of coarse SiC particles with  $Al_3BC$ .



**Figure 2.11.** The infiltration mechanism of  $B_4C$  - SiC - Al composite [15]

Zahedi et al. have worked to produce SiC - Al composites based on the SiC porous preforms by pressureless melt infiltration. Due to the non-wetting system of SiC - Al, pressure melt infiltration may be applied to assist the infiltration process. If the wetting condition is enhanced by adding preferably more than 3 wt. % magnesium to the aluminum melt and changing the internal atmosphere of the furnace to 100% nitrogen, pressureless melt infiltration may also be applied. Magnesium is an effective surfactant that clean oxygen from the melt surface. The formation of  $MgAl_2O_4$  provides the consumption of oxygen present in the atmosphere and decreases the thickness of the oxide layer. Hence, magnesium affects positively infiltration process by enhancing wetting behavior. Also, the used nitrogen atmosphere avoids the formation of the oxide layer and enhances wetting behavior [23].

### 2.5.2. Pressure Melt Infiltration

In pressure melt infiltration, firstly metal block is melted and sintered ceramic preform is preheated. The preform is placed inside the preheated die. Molten metal is poured and infiltrated under pressure. Then ejection and cooling are applied. Figure 2.12 shows the pressure melt infiltration process.

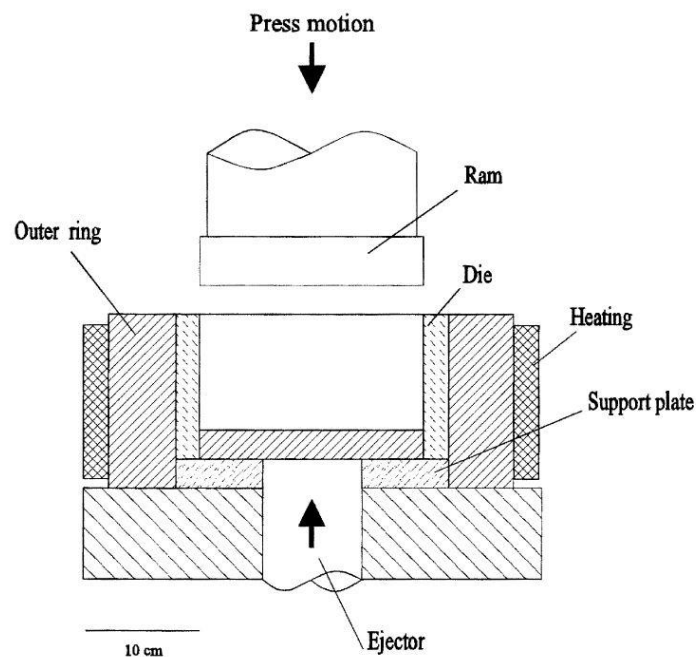


**Figure 2.12.** Illustration of the pressure melt infiltration [26]

SiC – Al composites are very difficult to produce by pressureless melt infiltration because of poor wetting system. It results in the presence of residual porosity because of poor wetting of silicon carbide by melted aluminum and the formation of undesirable reaction products  $Al_4C_3$ ,  $AlSiC_4$  due to the dissolution of the SiC by molten Al which decreases mechanical properties of the composite. Because these phases are developed at high temperatures ( $>660^\circ C$ ) and atmospheric pressure, SiC

becomes thermodynamically unstable and interfacial reactions take place. Also, these phases hydrolyze with the atmospheric humidity and resulted in the formation of  $\text{Al}(\text{OH})_3$  that causes crack propagation in composite via corrosion mechanism.  $\text{B}_4\text{C}$  addition provides enhancing wettability of  $\text{SiC}$  by  $\text{Al}$  [15]. Thus,  $\text{B}_4\text{C} - \text{SiC} - \text{Al}$  composites can be produced by pressureless melt infiltration process in which application of external pressure for filling of voids of ceramic preforms by liquid metal is not necessary. To produce  $\text{SiC} - \text{Al}$  composites, an external pressure should be applied to exceed threshold pressure which is the pressure required to handle capillary back pressure by pressure melt infiltration process [23].

Chedru et al. have worked to produce  $\text{AlN-Al}$  composites based on the  $\text{AlN}$  porous preforms by pressure melt infiltration. The whole infiltration process was ended in just 120 seconds. As a result of this study, the composite was considerably dense and microstructure showed homogeneous distribution of the aluminum and small amount of porosity. During this study different kind of aluminum alloys and pure aluminum were used as the infiltrated metal. Only pure aluminum failed that partial infiltration occurred. This study shows also that some infiltrating agents are required to achieve full infiltration [26].

H. S. Lee and S. H. Hong have worked to produce  $\text{SiC} - \text{Al}$  composites that contain high volume fraction  $\text{SiC}$  particles up to 70 vol. % by pressure melt infiltration. Two different kinds of  $\text{SiC}$  particles which particle sizes of 8  $\mu$  and 48  $\mu$ , 0 - 4 wt. % colloidal silica as inorganic binder and 1 wt. % cationic starch as organic binder were ball milled and then cold pressed at 1 - 2 MPa to have porous ceramic preforms. Preforms heated at 1100 °C for 4 hours.  $\text{Al}$  was melted and the temperature of the  $\text{Al}$  melt was kept between 700 °C and 800 °C. The preform was reheated to 450-550 °C. Molten  $\text{Al}$  was infiltrated by applying 10 -50 MPa. Importance of some parameters such as the temperature of molten  $\text{Al}$ , the temperature of preform before infiltration, infiltration pressure and infiltration time was emphasized. These parameters should

be controlled to avoid early solidification since it may cause the formation of pores and blockage of microstructure that means partial infiltration. The volume fraction of SiC could be controlled by controlling the particle sizes of SiC particles and their mixing ratio. The colloidal silica provided higher bond strength between contacting SiC particles since it transforms the cristobalite phase. As a result, H. S. Lee and S. H. Hong concluded that full infiltration may be achieved via process parameters such as the temperature of molten al 800 °C, the temperature of preform before infiltration 550 °C, infiltration time 20 -70 seconds, infiltration pressure 30-50 MPa [27].



## CHAPTER 3

### AIM OF THE STUDY

#### 3.1. MOTIVATION OF THE STUDY

In this thesis, the development of ceramic-metal FGM for defense applications was aimed. In defense applications, development of material with low density, high hardness at the impact point of the projectile and high flexural strength at the backing point are very important.  $B_4C$ ,  $SiC$  and  $Al$  which have low density were used to obtain lightweight armor material. FGM process that provides different mechanical properties at different sections was used to obtain both high hardness and high flexural strength in the same body. Figure 3.1 illustrates the expected structure and mechanical properties. The black part of the sample includes the highest number of ceramic particles, so hardness is the highest at that part. Gray part of the sample includes the highest number of metal particles, so flexural strength is the highest at that part. These mechanical properties increase or decrease gradually with gradually changing compositions (ceramic -metal ratio).

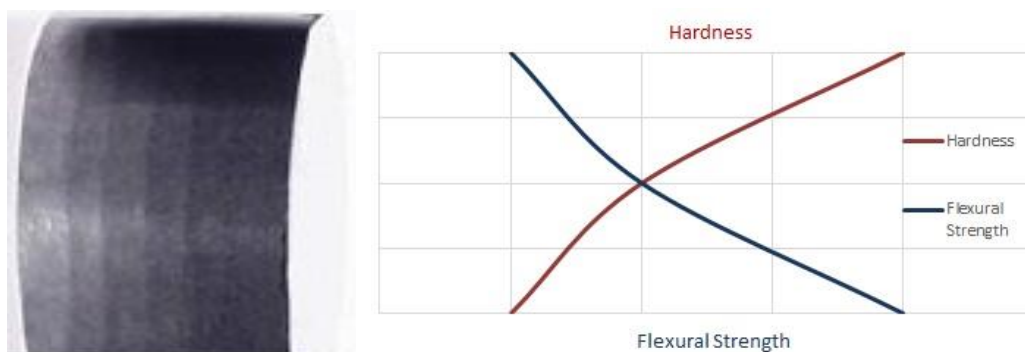


**Figure 3.1.** Expected structure and mechanical properties

Pressure melt infiltration process was applied to produce near or near-net shape ceramic-metal FGM. High ceramic fraction composites were produced at lower temperature, 1400 °C without  $Al_4C_3$  phase formation which is detrimental. Since the cost of  $B_4C$  is higher than the cost of SiC,  $B_4C$ -SiC-Al composites which contain low  $B_4C$  wt. % were produced. Also, it was aimed that composite exhibits low density and high hardness despite decreasing wt. % of  $B_4C$ .

### **3.2. MAIN CONTRIBUTION TO THE LITERATURE**

FGM can be considered as a potential candidate for armor applications since it exhibits different mechanical properties at different parts of the material. Thus, a combination of two contrasting properties which are high hardness and high flexural strength in the same body can be obtained. With this thesis, a new kind of material that can be used for defense applications was produced.

In conventional ballistic plates, ceramic plates are joined to metal or polymer layers. Because differences between thermal expansion coefficients of ceramics and metals/polymers are high, a combination of them without gradient may result in residual stress, unjoined edges, unjoined pores, reaction layer with cracks which are detrimental for armor applications. By the FGM process, difficulties of the joining of dissimilar materials were overcome by gradually changing composition so mechanical properties.

$B_4C$  does not provide effective protection against armor piercing projectiles because of the amorphization process. It is a good candidate for one-hit protection. When multi-hit protection is required SiC whose hardness is close to that of  $B_4C$  can be used. Also, adding metal to composite improves the flexural strength of the plate, so increases penetration resistance.

## CHAPTER 4

### EXPERIMENTAL PROCEDURE

In this chapter, the production of  $B_4C - SiC - Al$  composites by pressure melt infiltration of ceramic preforms with aluminum alloy are explained. Also, applied characterization methods are indicated. Figure 4.1 shows the experimental flow chart.

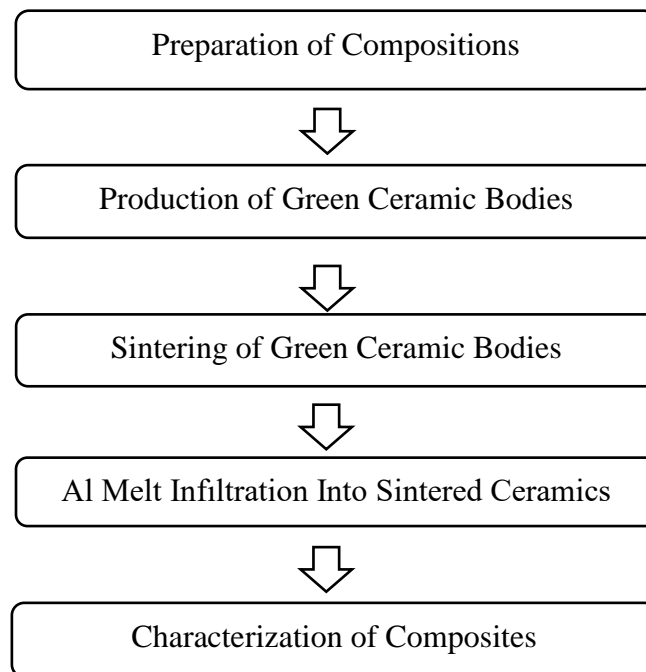


**Figure 4.1.** Experimental flow chart

#### 4.1. PRODUCTION OF FGM LAYERS

In this thesis, firstly each potential layer of FGM was produced separately to investigate the effects of each layer to the composite in terms of green/bulk density, porosity, microstructure and some mechanical properties. In the light of the literature review, at least 10 wt. % of B<sub>4</sub>C is required as sintering aids. 10 wt. % of Al<sub>2</sub>O<sub>3</sub> was used at all layers to provide higher penetration and abrasion resistance. The composition is the most important variable to obtain gradual changing green/bulk density and/or porosity which are the requirements of an FGM sample. So, it was planned to prepare compositions to create each layer of FGM which is indicated in Table 4.1.

**Table 4.1.** The Layers of FGM

Layers	Composition	B <sub>4</sub> C (weight %)	SiC (weight %)	Al <sub>2</sub> O <sub>3</sub> (weight %)
1	80S10B10A	10	80	10
2	70S20B10A	20	70	10
3	60S30B10A	30	60	10

B<sub>4</sub>C powders which have 1 μm (d<sub>50</sub>) particle size, SiC powders which have 35 μm (d<sub>50</sub>) particle size and Al<sub>2</sub>O<sub>3</sub> powders which have 6 μm (d<sub>50</sub>) particle size were used. To obtain a green body, all the ceramic particles, 15 wt. % PVA or PEG as binders and 1 wt. % Cu-Zn stearate as lubricant were mixed by ball milling in alcohol media. Three different compositions in Table 4.1. which indicated wt. % of B<sub>4</sub>C, SiC and Al<sub>2</sub>O<sub>3</sub> ceramic particles were produced separately. PVA or PEG solution was prepared by mixing 50 ml of boiled distilled water with 5 grams of PVA or PEG powder until completely dissolved. The amount of zirconia ball and the amount of alcohol was equal to the amount of total ceramic powders. Ball milling operation was applied for 90 minutes. Figure 4.2 illustrates ball milling machine and jar filled with ingredients.

When ball milling operation finished, the milled solution was poured into a beaker and then beaker was placed in a furnace and operated to remove alcohol and water in milled solution. Thus, the preparation of the compositions section was completed.



**Figure 4.2.** Ball milling machine and jar filled with ingredients

Ceramic preforms were produced by pressing operation which involves the compaction of powder into a rigid die by applying pressure in a single axial direction through a rigid punch or piston. Before pressing operation, 15 ml glucose - distilled water solution which has 50 wt. % glucose was added to the composition to provide moisture and binding. The manual press was applied under 70 tons pressure and it means that green ceramic bodies were produced under 100 MPa pressure according to dimensions of the mold. Width and length of the sample depend on dimensions of the mold which is cylindrical with 9 mm diameter; whereas the height of the sample depends on the weight of composition pressed. Pressed samples were kept at room temperature at least one day to release their humidity before sintering operation. Thus, the production of green ceramic bodies section was completed. Figure 4.3 illustrates pressing operation and green ceramic body.



**Figure 4.3.** Pressing operation and green ceramic body

Due to compacts with high amounts of binder decreases mechanical properties of the ceramic preform and may affect the sintering process negatively, the binder should be removed prior to sintering. Debinding process at 550 °C for 2 hours followed by the sintering process at 1400 °C for 2 hours were done in a nitrogen atmosphere by using Protherm furnace. The heating rate was applied 3 °C / min until 550 °C, 5 °C / min until 900 °C and 10 °C / min until sintering temperature which is 1400 °C. Thus, the sintering of green ceramic bodies section was completed. Figure 4.4 shows furnace and temperature vs time graph of the sintering process.

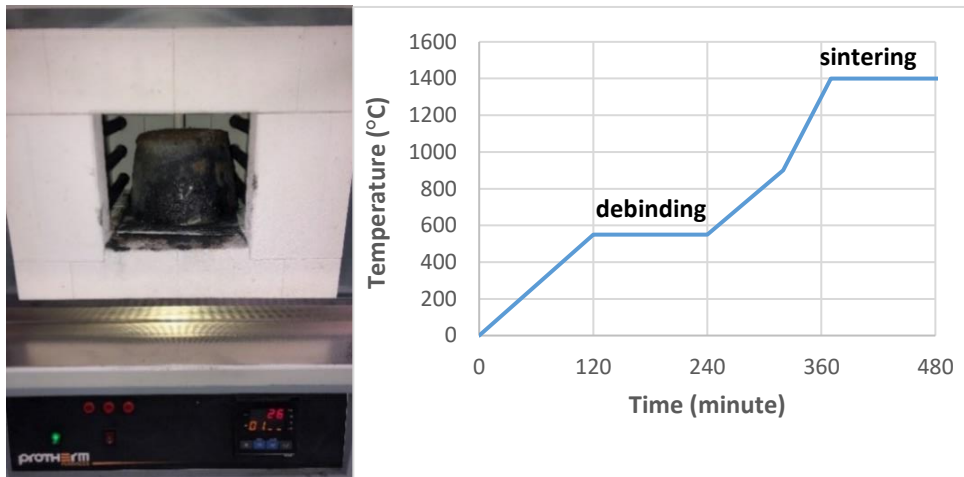


**Figure 4.4.** Furnace and temperature vs time graph of the sintering process

Due to the problem encountered at the sintering process because of  $\text{Al}_2\text{O}_3$  ceramic powder, it was planned to prepare new compositions to create each layer of FGM which is indicated in Table 4.2. All the experimental procedure was followed as before except for rectangular mold which has 120 mm X 40 mm dimensions used for pressing and melt infiltration process with an applied pressure of 200 MPa. More pressure could be achieved by double action press. 100 tons of pressure could be applied and it means that ceramic green bodies were produced under 200 MPa pressure.

**Table 4.2.** The Layers of FGM

Layers	Composition	$\text{B}_4\text{C}$ (weight %)	$\text{SiC}$ (weight %)
1	90S10B	10	90
2	80S20B	20	80
3	70S30B	30	70

The porosity of the sintered ceramic bodies should be filled with metal to reach near theoretical density. It was achieved by the pressure melt infiltration process which is illustrated in Figure 4.5. After Al alloy was melted, the sintered ceramic preform was

preheated to 900 °C. Preform placed inside the preheated die on alumina thermal paper to decrease temperature differences between metal mold and liquid metal. Molten aluminum alloy was poured at 700 °C and infiltrated under 200 MPa pressure. Then ejection and cooling were applied.

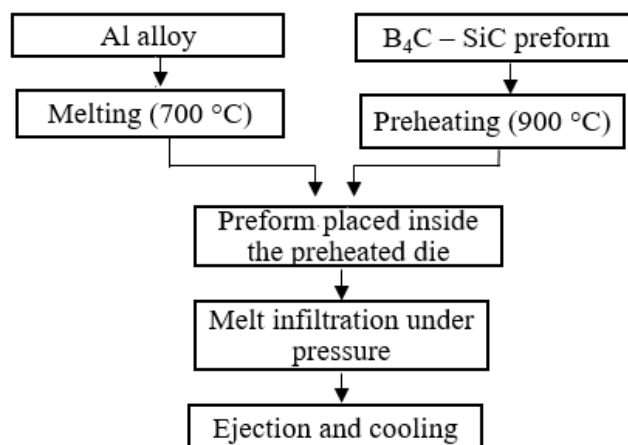


**Figure 4.5.** Pressure melt infiltration process

7075 Al alloy is widely used as infiltrated metal in literature due to its low melting point, low density and high ductility. The new composition was developed by adjusting 7075 Al alloy with 11,2 wt. % Si and 6,9 wt. % Mg to increase the infiltration rate in the light of the literature review as illustrated in Figure 4.6. Silicon addition increases Al alloy's fluidity and decreases its melting temperature. Silicon prevents interfacial reactions between SiC and Al. While magnesium reduces the surface tension and the wetting angle between Al melt and B<sub>4</sub>C – SiC ceramics. Magnesium vaporizes from Al melt as a result of high gas pressure and it may destroy the Al<sub>2</sub>O<sub>3</sub> layer on the surface of Al alloy and helps direct contact between the Al melt and B<sub>4</sub>C – SiC ceramics.



**Figure 4.6.** Preparation of new Al alloy

Thus, Al melt infiltration into the sintered ceramic section was completed. Figure 4.7 shows preheated die and 90S10B composite after aluminum pressure melt infiltration process.



**Figure 4.7.** Preheated die and 90S10B composite after aluminum pressure melt infiltration process

## **4.2. PRODUCTION OF FGM**

After investigating the effects of each layer to the composite in terms of green/bulk density, porosity, microstructure and some mechanical properties, FGM with different compositions which are indicated in Table 4.2 was produced. All the experimental procedure was followed as before. Green ceramic bodies were produced by respectively addition and pressing of each composition as layers of FGM. Before pressing operation, 5 ml glucose - distilled water solution which has 50 wt. % glucose was added to each composition to provide moisture and binding.

## **4.3. CHARACTERIZATION OF COMPOSITES**

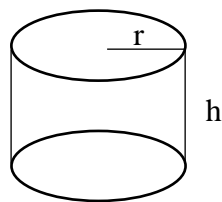
The composites were characterized by phase analysis, particle size and distribution analysis, green and bulk density/porosity measurement, optic emission spectrometer analysis, XRD analysis, optical microscopy and SEM-EDX analyses, hardness measurement and three point bend test.

For sample preparation, composites were cut with silicon carbide cutting disc into required dimensions. Mounting was done by bakelite powder. After that, samples were ground by abrasive papers with different grids and polished by broadcloths with diamond solutions with 6 and 1  $\mu$  particle size respectively.

Particle size and distribution analysis is important in terms of creating compositions which result in different green/bulk density and so porosity. It was done to each composition of each layer after ball milling operations with the Malvern Mastersizer 2000 device. This device also provides specific surface areas of each composition.

Green density measurement was done to evaluate how tightly packed the powder particles. Green densities of each layer were calculated, so whether gradual changing green density for FGM was obtained or not could be understood.

For green ceramic bodies produced by manual press, the calculation is as indicated in Equation 4.1 according to cylindrical mold where  $r = 4,5 \text{ cm}$  ,  $d_{B4C} = 2,52 \text{ g/cm}^3$  ,  $d_{SiC} = 3,21 \text{ g/cm}^3$ :



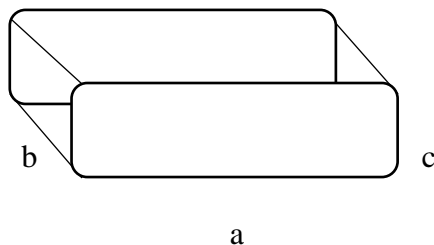
$$V_{\text{obtained}} = \pi \cdot r^2 \cdot h$$

$$V_{\text{theoretical}} = ( m_{B4C} / d_{B4C} ) + ( m_{SiC} / d_{SiC} )$$

$$\% d_{\text{green}} = ( V_{\text{theoretical}} / V_{\text{obtained}} ) \cdot 100$$

**Equation 4.1.** Green density calculation for manual pressed green ceramic bodies

For green ceramic bodies produced by double action press, the calculation is as indicated in Equation 4.2 according to rectangular mold where  $a = 12 \text{ cm}$  ,  $b = 4 \text{ cm}$  ,  $d_{B4C} = 2,52 \text{ g/cm}^3$  ,  $d_{SiC} = 3,21 \text{ g/cm}^3$ :



$$V_{\text{obtained}} = a \cdot b \cdot c$$

$$V_{\text{theoretical}} = ( m_{B4C} / d_{B4C} ) + ( m_{SiC} / d_{SiC} )$$

$$\% d_{\text{green}} = ( V_{\text{theoretical}} / V_{\text{obtained}} ) \cdot 100$$

**Equation 4.2.** Green density calculation for double action pressed green ceramic bodies

Bulk density and porosity measurements were done by Archimedes principle to evaluate the required amount of Al alloy for each composition to reach near theoretical density and amount of porosity after the infiltration process. The theoretical density of each layer was calculated according to the rule of mixture to use them in porosity (%) formula given in Figure 4.11, so whether gradual changing porosity percentage for FGM was obtained or not could be understood.

Archimedes principle was applied with xylene solution to determine the bulk density and porosity % of sintered layers of FGM. Firstly, samples were weighed as dry which is termed as  $m_{dry}$ . Then, after samples were kept in xylene solution for 24 hours, samples were weighed in xylene solution which is termed as  $m_{submerged}$ . Finally, samples were extracted from the solution, the surfaces of the samples were wiped out and the samples were weighed in the air which is termed as  $m_{wet}$ . Density of xylene solution is  $0,861 \text{ g/cm}^3$ . Calculations of bulk density ( $d_{bulk}$ ) and porosity (P) % are illustrated in Equation 4.3.

$$V = ( m_{wet} - m_{submerged} ) / 0,861$$

$$d_{bulk} = m_{dry} / V$$

$$P (\%) = [ (\text{theoretical density} - \text{bulk density}) / \text{theoretical density} ] \times 100$$

**Equation 4.3.** Calculation of bulk density and porosity % by using xylene solution

Archimedes principle was applied with distilled water to determine the bulk density and porosity % of Al alloy infiltrated FGM. Firstly, samples were weighed as dry which is termed as  $m_{dry}$ . Then, after samples were boiled in distilled water for 1 hour and cooled to room temperature, samples were weighed in distilled water which is termed as  $m_{submerged}$ . Finally, samples were extracted from distilled water, the surfaces

of the samples were wiped out and the samples were weighed in the air which is termed as  $m_{\text{wet}}$ . Calculations of bulk density ( $d_{\text{bulk}}$ ) and porosity (P) % are illustrated in Equation 4.4.

$$d_{\text{bulk}} = m_{\text{dry}} / (m_{\text{wet}} - m_{\text{submerged}})$$

$$P (\%) = [ (m_{\text{wet}} - m_{\text{dry}}) \times 100 ] / (m_{\text{wet}} - m_{\text{submerged}})$$

**Equation 4.4.** Calculation of bulk density and porosity % by using distilled water

The composition of Al alloy used for pressure melt infiltration process was measured with optic emission spectrometer analysis. The results are given as weight percentage. The composition analysis was carried out by WAS Foundry Master after alloy preparation in the induction furnace.

Processes used in this thesis study may yield a mixture of several ceramic and metal phases that differ from the starting materials. XRD measures reaction products (phases) formed. With this technique formation of  $\text{Al}_4\text{C}_3$  which is a detrimental phase and other phases can be investigated. Reference pdf cards were used to detect which peaks belong to which phases. XRD analysis was applied by using the Bruker D8 Advance device after breaking up composites into small particles. Samples were scanned with  $1^\circ/\text{min}$  speed between  $20^\circ$  and  $80^\circ$ .

Optical microscopy was used to examine microstructure and to do phase analysis. During phase analysis, different colors created for different phases thanks to contrast differences. SEM analysis was done for microstructural examination in high magnifications and resolutions. Microscope analysis provides to see the gradual

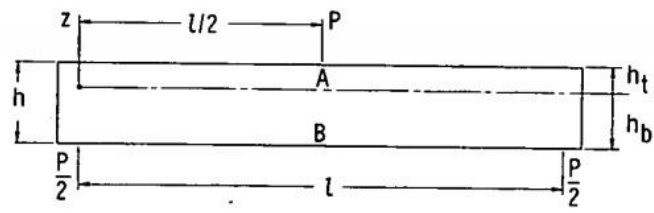
changing of microstructure between each layer of FGM. Quantitative phase analysis was conducted using EDS.

Three point bend tests and hardness measurements were applied for each layer separately to determine the effect of each layer to the flexural strength and hardness. Hardness and flexural strength of each layer were detected, so whether gradual changing hardness and flexural strength for FGM was obtained or not could be understood. Hardness values were calculated in the HRC scale by using 150 kg load. Three point bend tests were done to evaluate the bending and fracture behavior of the Al alloy and composites by using Instron 5582 tensile test machine. Calculations of flexural strength are given in Equation 4.5. The letters M, c, I, F, L, w, h represent bending moment, area moment of inertia, distance from neutral plane, load at span center, distance between supports (80 mm), width (40 cm) and height of the specimen respectively. Specimen subjected to three point bend test and stress/strain variations are illustrated in Figure 4.8. The material remains unstressed at the transition from tensile to compressive stress. This transition plane is called as neutral plane. Neutral plane for ceramic metal composite is the interlayer between ceramic and metal.  $h_b$  is measured from the neutral plane to the bottom of the specimen (metal part) and  $h_t$  is measured from the neutral plane to the top of the specimen (ceramic part). When  $h_b = h_t$ ,  $c=h/2$ .

$$\sigma = ( M \cdot c ) / I \text{ where; } M = ( F \cdot L ) / 4, I = ( w \cdot h^3 ) / 12 \text{ and } c = \text{distance from neutral plane} \quad (a)$$

$$\sigma = 1,5 \cdot ( F \cdot L ) / ( w \cdot h^2 ) \quad (b)$$

**Equation 4.5.** (a) Calculation of flexural strength, (b) Calculation of flexural strength when  $c = h/2$



(a) Specimen geometry.

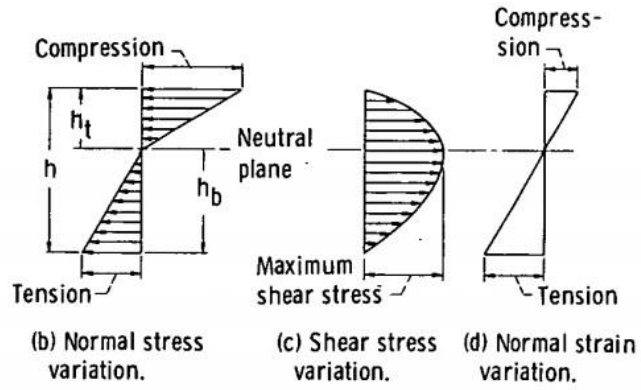


**Figure 4.8.** (a) Specimen geometry, (b) Normal stress variation, (c) Shear stress variation, (d) Normal strain variation [31]



## CHAPTER 5

### RESULTS AND DISCUSSION

#### 5.1. PHASE ANALYSES

Phase analyses were done by Thermo-Calc software. B<sub>4</sub>C-SiC composites at 1400 °C temperature were investigated by drawing ternary phase diagrams by selecting B, C and Si elements. Figure 5.1 shows that there are B<sub>4</sub>C and SiC phases in solid state at each composition which are 90S10B, 80S20B and 70S30B.

The mass percent of elements were calculated for each composition. For example, Figure 5.2 shows the calculation of mass percent of elements in 90S10B composition which includes 10 wt. % B<sub>4</sub>C and 90 wt. % SiC. According to that calculation, 90S10B composition includes 7.8 weight % B, 63.1 weight % Si and 29.1 weight % C elements. The interception point of two elements (C and Si) in this figure represents the phase region.

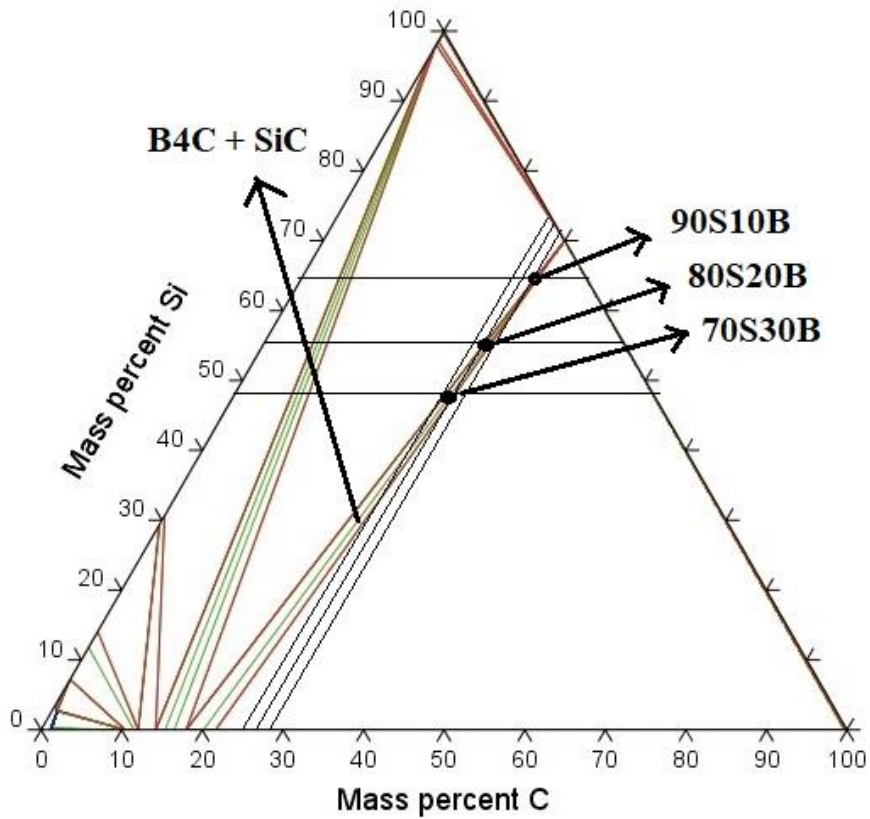


**Figure 5.1.** Ternary phase diagram of B, C and Si elements at 1400 °C

$$\text{B}_4\text{C} \longrightarrow 4 \times M_{\text{B}} + M_{\text{C}} = 43.2 + 12 = 55.2$$

$$\text{SiC} \longrightarrow M_{\text{Si}} + M_{\text{C}} = 28.1 + 12 = 40.1$$

$$\text{Mass percent B} = (10 \times 43.2) / 55.2 = 7.8$$

$$\text{Mass percent Si} = (90 \times 28.1) / 40.1 = 63.1$$

$$\text{Mass percent C} = 100 - (7.8 + 63.1) = 29.1$$

**Figure 5.2.** Calculation of mass percent of elements in 90S10B composition

Al alloy at 700 °C temperature was investigated by drawing ternary phase diagrams by selecting Al, Mg and Si elements. The Al alloy includes 74,2 wt. % Al, 11,2 wt. % Si and 6,9 wt. % Mg elements. The interception point of two elements (Al and Si) in Figure 5.3 shows the phase region which is the liquid phase. Thus, 700 °C was chosen as molten metal temperature for the infiltration process.

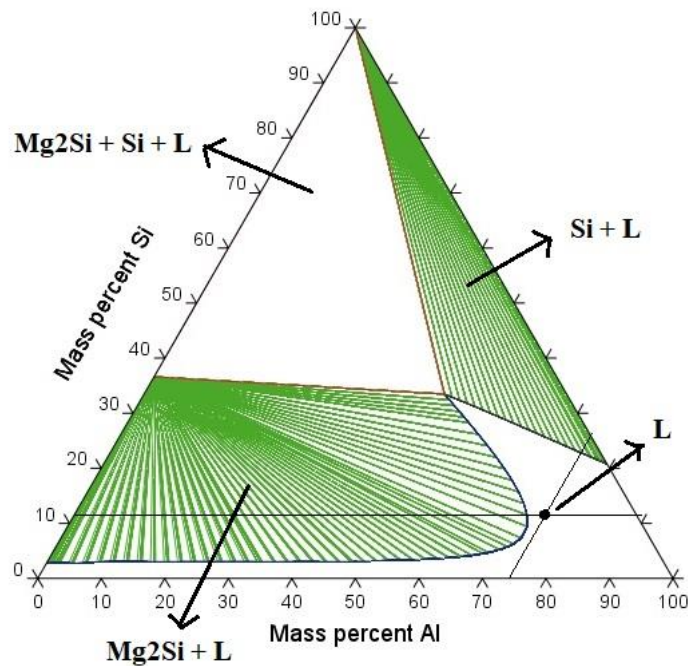


**Figure 5.3.** Ternary phase diagram of Al, Mg and Si elements at 700 °C

## 5.2. PARTICLE SIZE AND DISTRIBUTION ANALYSIS

Composite with high ceramic fraction is required for armor applications. To reach high green densities, high coordination number which is defined as the number of particles that a particle holds as its nearest neighbors in a coordination compound is required. In this thesis, B<sub>4</sub>C powders which have 1 μm particle size and SiC powders

which have 35  $\mu\text{m}$  particle size were ready to use. To get high coordination number  $\text{Al}_2\text{O}_3$  powders which have 6  $\mu\text{m}$  particle size were procured.

Particle size and distribution analyses are illustrated in Figure 5.4, 5.5 and 5.6 for 90S10B, 80S20B, 70S30B respectively. There are two peaks and they are called bimodal because there are both fine grain size  $\text{B}_4\text{C}$  and coarse grain size  $\text{SiC}$ . Also, particle size distribution is wide.

We can see from these figures that as  $\text{B}_4\text{C}$  content increases from 10 wt. % to 20 wt. %, the intensity of first peaks on the left side increases because  $\text{B}_4\text{C}$  has smaller particle size. 80S20B composition has the highest first peak among them. Also, we can see from these figures that as  $\text{SiC}$  content increases from 80 wt. % to 90 wt. %, the intensity of second peaks on the right side increases because  $\text{SiC}$  has larger particle size. 90S10B composition has the highest second peak among them. It was concluded that these results may be wrong because  $\text{B}_4\text{C}$  has smaller particle size than  $\text{SiC}$ , the intensity of first peak should increase and the intensity of second peak should decrease as  $\text{B}_4\text{C}$  content increases from 20 wt. % to 30 wt. These may result from agglomeration of 70S30B composition and some measuring errors of device.

The  $d(0,5)$  is the diameter of the particle that 50% of a sample's mass is smaller than and 50% of a sample's mass is larger than. The  $d(0,5)$  is also known as the "mass median diameter" as it divides the sample equally by mass. We can see from these figures that as  $\text{B}_4\text{C}$  content increases from 10 wt. % to 20 wt. %,  $d(0,5)$  value dramatically decreases from 27.23  $\mu\text{m}$  to 3.30  $\mu\text{m}$ , because  $\text{B}_4\text{C}$  has lower particle size. 80S20B composition has the lowest  $d(0,5)$  value among them. However, as  $\text{B}_4\text{C}$  content increases from 20 wt. % to 30 wt. %,  $d(0,5)$  value slightly increases from 3.30  $\mu\text{m}$  to 5.02  $\mu\text{m}$ .



Particle size and distribution analysis also provides specific surface area. Table 5.1 shows the specific surface area of each composition. Specific surface area increases from 1.3 m<sup>2</sup>/g to 2.78 m<sup>2</sup>/g as B<sub>4</sub>C content increases from 10 wt. % to 20 wt. %. But the specific surface area decreases as B<sub>4</sub>C content increases from 20 wt. % to 30 wt. % in spite of increasing wt. % of B<sub>4</sub>C which has smaller particle size. That result was supported by d(0.5) values of these compositions. Figure 5.7 shows the variation of d(0.5) values of each composition with respect to B<sub>4</sub>C content. Figure 5.8 shows the variation of the specific surface area of each composition with respect to B<sub>4</sub>C content. It was concluded that these results may be wrong because B<sub>4</sub>C has smaller particle size than SiC, d(0.5) value should decrease and specific surface area should increase as B<sub>4</sub>C content increases from 20 wt. % to 30 wt. These may result from agglomeration of 70S30B composition and some measuring errors of particle size and distribution analysis device.

**Table 5.1.** Specific surface area of compositions

Composition	Specific Surface Area (m <sup>2</sup> /g)
90S10B	1.3 (± 0,02)
80S20B	2.78 (± 0,01)
70S30B	2.17 (± 0,04)

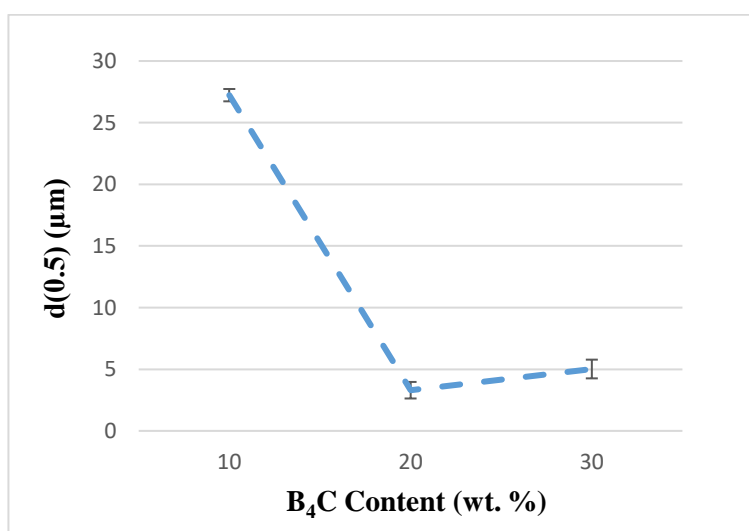


**Figure 5.7.** Variation of d(0.5) values with respect to B<sub>4</sub>C content

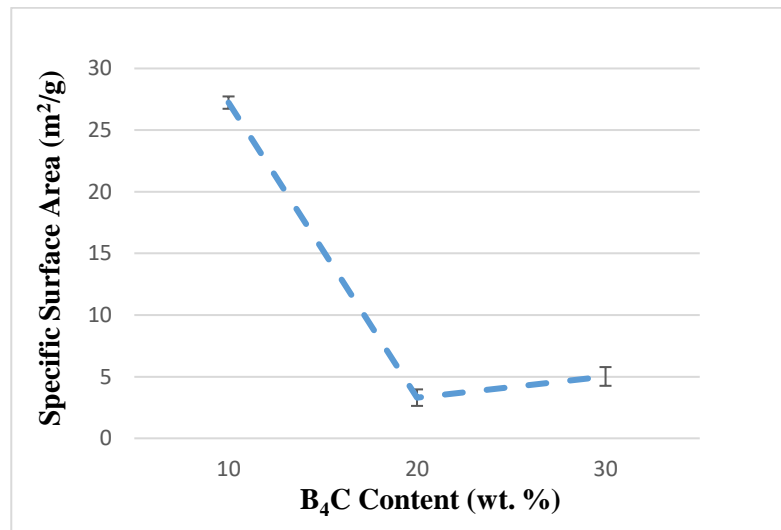


**Figure 5.8.** Variation of specific surface area values with respect to B<sub>4</sub>C content

### **5.3. GREEN DENSITY AND BULK DENSITY / POROSITY MEASUREMENTS**

Green densities of each composition were calculated as mentioned in Section 4.3. To obtain nearly accurate green density value, four ceramic green bodies of each composition were prepared and green density results averaged as shown in Table 5.2. Green density varies according to composition because of the changing weight percentage of fine B<sub>4</sub>C particles and coarse SiC particles. Figure 5.9 shows green density variation with B<sub>4</sub>C content. As B<sub>4</sub>C wt. % increases from 10 to 20, green density increases dramatically while further addition up to 30 wt. % leads to a slight increment in green density. That result was supported with d(0.5) values and specific surface area of each composition. In conclusion, it was understood that green density values increase from 90S10B composition to 70S30B composition to obtain FGM. However, the increment is not gradual.

**Table 5.2.** Green densities of each composition

Composition	Green Density (%)
90S10B	62,78 ( $\pm 0,63$ )
80S20B	68,03 ( $\pm 0,55$ )
70S30B	68,08 ( $\pm 0,63$ )

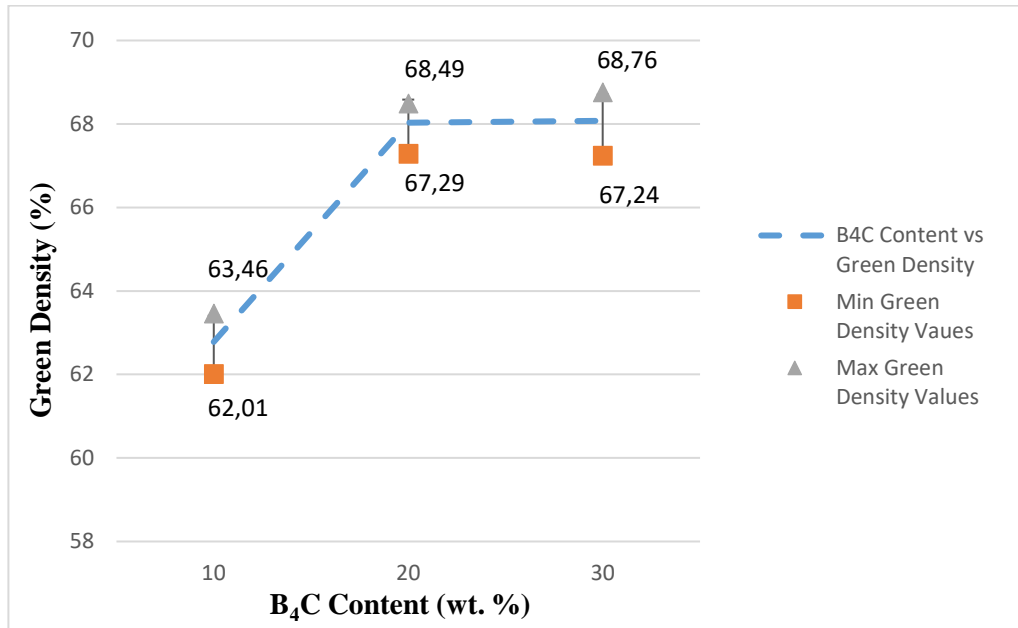


**Figure 5.9.** Green density variation with B<sub>4</sub>C content

Bulk density and porosity % of each sintered layer of FGM were calculated as mentioned in Section 4.3. To obtain nearly accurate bulk density and porosity % value, three pieces of samples were prepared. The theoretical density of each layer was calculated according to the rule of mixture, then porosity % of each layer was determined with formula by using theoretical and bulk density values as shown in Table 5.3. Figure 5.10 shows porosity % variation with B<sub>4</sub>C content. As B<sub>4</sub>C wt. % increases from 10 to 20 and 20 to 30, porosity % decreases gradually from 34,2 to 29,6 and 29,6 to 23,2 respectively. However gradual changing of green density from 80S20B layer to 70S30B layer could not be achieved, gradual changing of bulk density/porosity % from 80S20B layer to 70S30B layer could be achieved due to

increment in wt. % of B<sub>4</sub>C that is densification aid. In conclusion, the gradual changing of porosity % from 90S10B layer to 70S30B layer to obtain FGM was achieved.

**Table 5.3.** Porosity % values of each composition

Composition	Theoretical Density (g/cm <sup>3</sup> )	Bulk Density (g/cm <sup>3</sup> )	Porosity %
90S10B	3,13	2,06 (± 0,03)	34,2 (± 0,91)
80S20B	3,04	2,14 (± 0,02)	29,6 (± 1,21)
70S30B	2,97	2,28 (± 0,03)	23,2 (± 0,88)

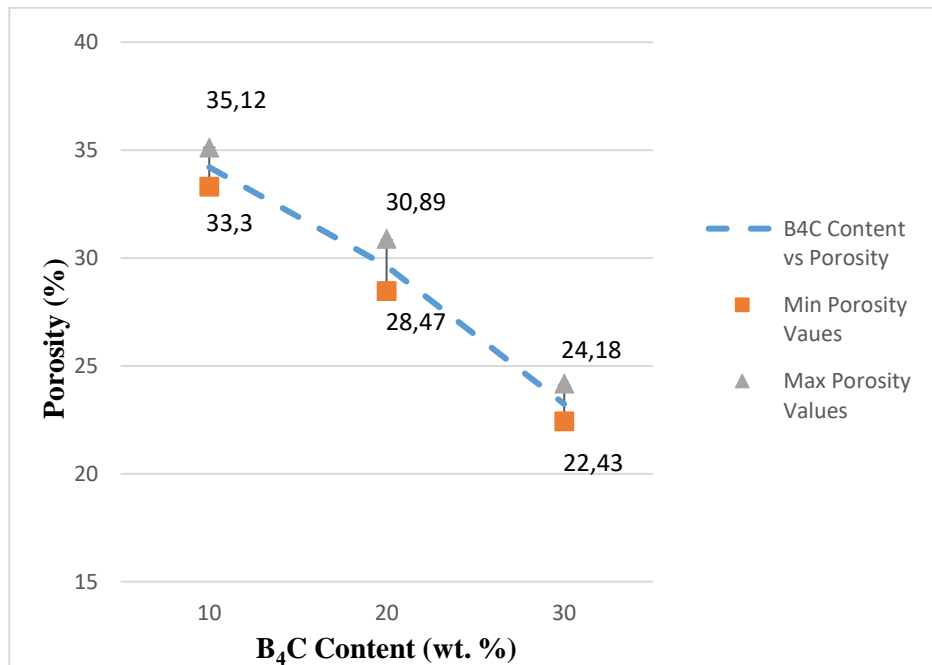


**Figure 5.10.** Porosity % variation with B<sub>4</sub>C content

In the light of these analyses, it was noted that FGM in Table 4.3 can be considered as a potential candidate for this study because as bulk density increases/porosity % decreases from 90S10B layer to 70S30B layer, amount of Al alloy to achieve full infiltration decreases from 90S10B layer to 70S30B layer.

Bulk density and porosity % of Al alloy infiltrated FGM were calculated as mentioned in Section 4.3. To obtain nearly accurate bulk density and porosity % value, three pieces of samples were prepared. Bulk density of FGM was calculated as 2,70 ( $\pm 0,02$ ) g/cm<sup>3</sup>. FGM was successfully infiltrated with porosity % lower than 0,88 ( $\pm 0,3$ ).

#### 5.4. OPTIC EMISSION SPECTROMETER ANALYSIS

During this study, the new Al alloy was produced from 7075 Al alloy. In the light of the literature review, it was aimed to use Al alloy with 4-8 wt. % Mg and up to 12 wt. % Si for pressure melt infiltration process to increase the infiltration rate. 7075 Al alloy was melted and required Mg and Si elements were added to the melt. Table 5.5 shows optic emission spectrometer analysis results of 7075 Al alloy and new composition which was modified from 7075 Al alloy for this study. The chemical composition of the new composition which was modified from 7075 Al alloy could be arranged as aimed.

**Table 5.4.** Optic emission spectrometer analysis results of 7075 Al alloy and new composition which was modified from 7075 Al alloy for this study

<u>Elements</u>	<u>Weight Percentage of Elements</u>	
	<b>7075 Al Alloy</b>	<b>New Composition</b>
<b>Al</b>	89,42 ( $\pm 0,32$ )	74,2 ( $\pm 0,7$ )
<b>Mg</b>	2,12 ( $\pm 0,05$ )	6,9 ( $\pm 0,5$ )
<b>Si</b>	0,27 ( $\pm 0,03$ )	11,2 ( $\pm 0,2$ )

#### 5.5. XRD ANALYSIS

During this thesis, some problems occurred due to Al<sub>4</sub>C<sub>3</sub> phase formations which are illustrated in Figure 5.11 with peaks represented by triangle shape as a result of XRD

analysis.  $\text{Al}_2\text{O}_3$  reacts with carbide-based ceramics such as  $\text{B}_4\text{C}$  and  $\text{SiC}$  at prolonged temperatures higher than  $1000\text{ }^\circ\text{C}$  and  $\text{Al}_4\text{C}_3$  phase formation occurs.  $\text{Al}_4\text{C}_3$  is very detrimental since it hydrolyzes with atmospheric moisture and  $\text{Al}(\text{OH})_3$  forms according to reactions illustrated in Equation 5.1. 80S10B10A sample was sintered, then was put into water. Some bubbles were observed and then the sample crashed into pieces as seen in Figure 5.12. Thus, it was decided to not to add  $\text{Al}_2\text{O}_3$  powder.

▲  $\text{Al}_4\text{C}_3$

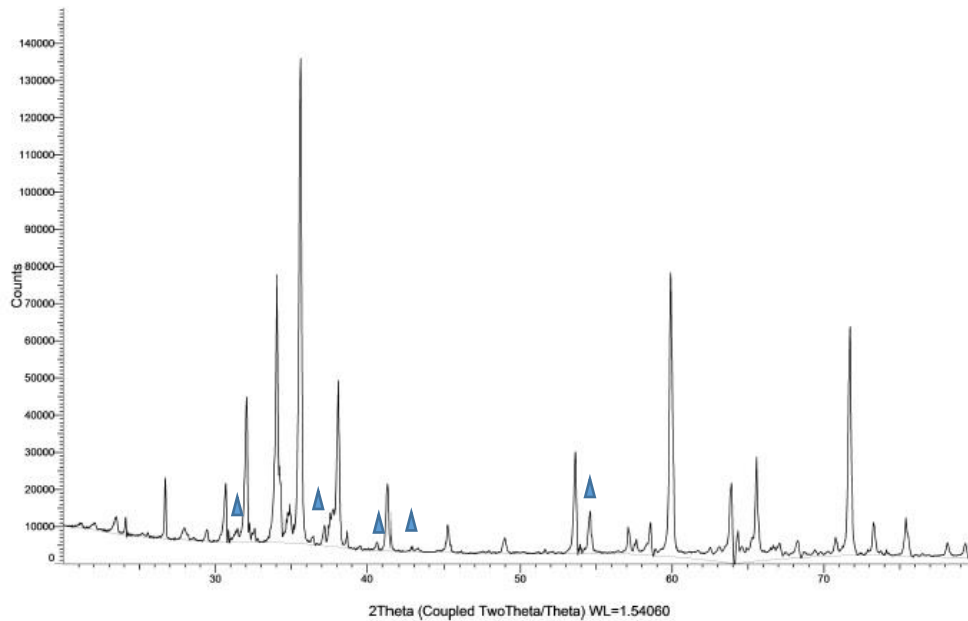


**Figure 5.11.** XRD analysis of sintered 80S10B10A



$$\Delta G^\circ_{1100} = -293.9 \text{ kJ/mol}$$



$$\Delta G^\circ_{1100} = -634.6 \text{ kJ/mol}$$

**Equation 5.1.**  $\text{Al}_4\text{C}_3$  and  $\text{Al}(\text{OH})_3$  formation reactions

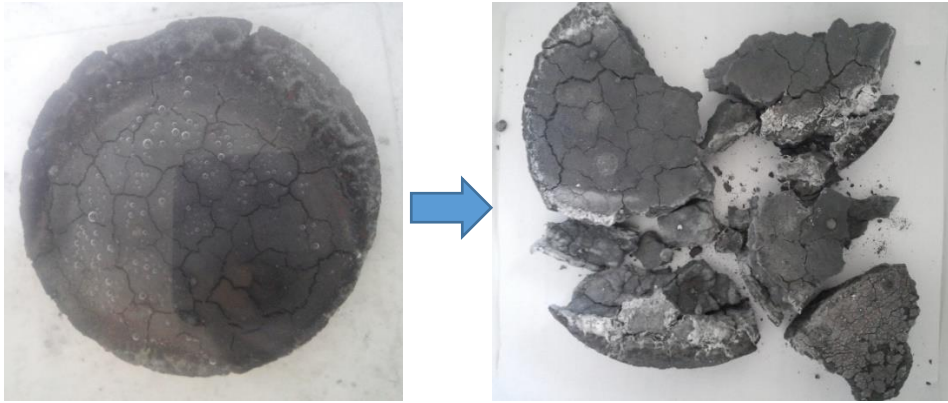


**Figure 5.12.** 80S10B10A sample was put into water and crashed

XRD analyses were applied to Al alloy and Al alloy infiltrated 70S30B, 80S20B, 90S10B, FGM composites which are illustrated in Figure 5.13, 5.14, 5.15, 5.16 and 5.17 respectively. For Al alloy used in this thesis study,  $Mg_2Si$  peaks were detected in addition to 7075 Al alloys peaks because the weight percentage of Mg and Si of new composition was higher than that of 7075 Al alloy and cause to formation of  $Mg_2Si$  phase. For Al alloy infiltrated 70S30B, 80S20B, 90S10B, FGM composites, no phases other than  $B_4C$ , SiC, Al,  $Mg_2Si$  and Si were formed. In this thesis, it was aimed that  $B_4C$  and SiC ceramic particles do not react with Al alloy in order to avoid the formation of intermetallic phases which decrease hardness of composite and formation of  $Al_4C_3$  which hydrolyzes with atmospheric moisture. These figures confirm that this aim was achieved.

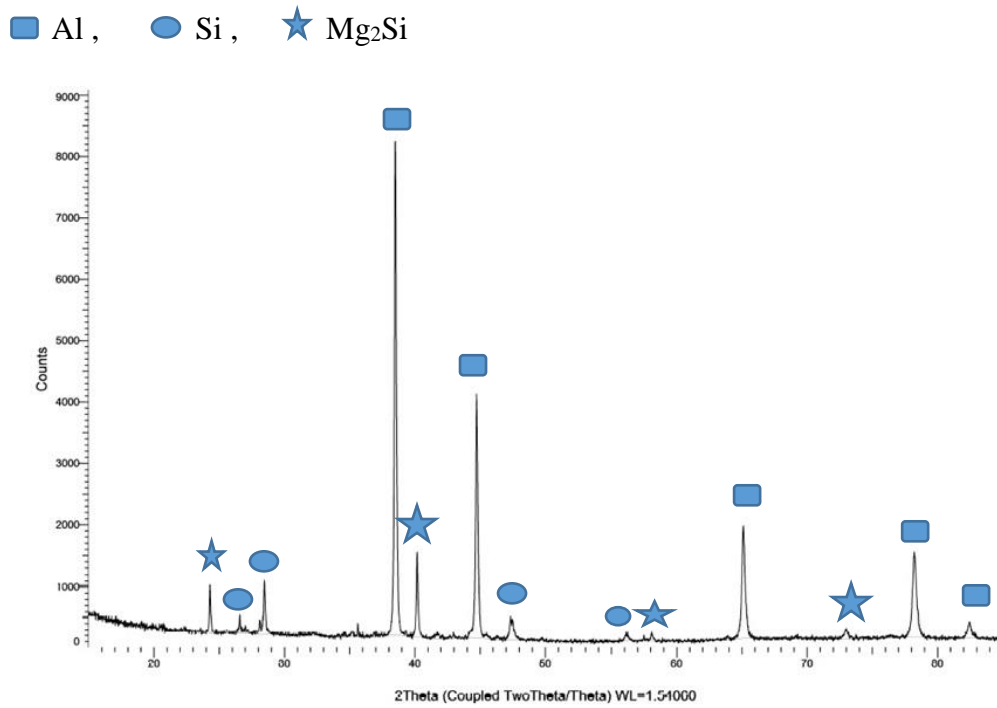


Figure 5.13. XRD analysis of Al alloy

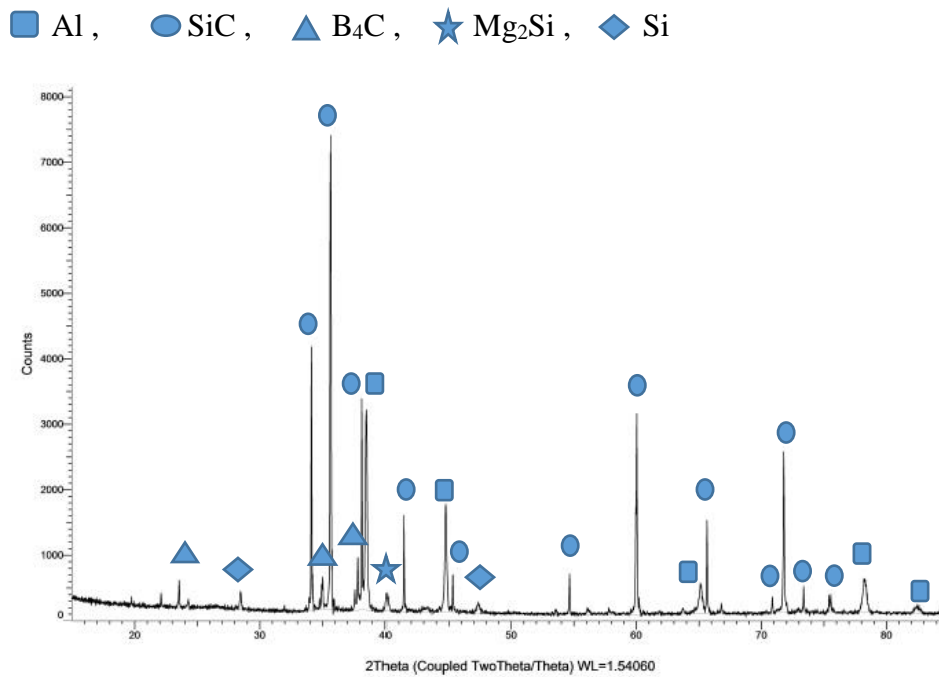
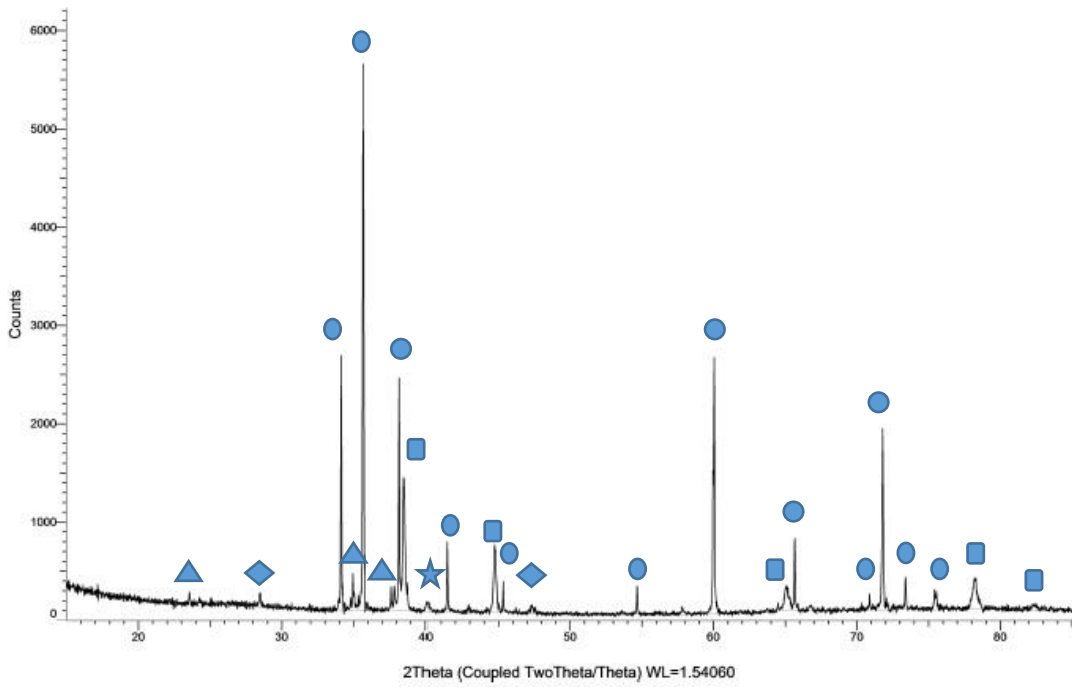
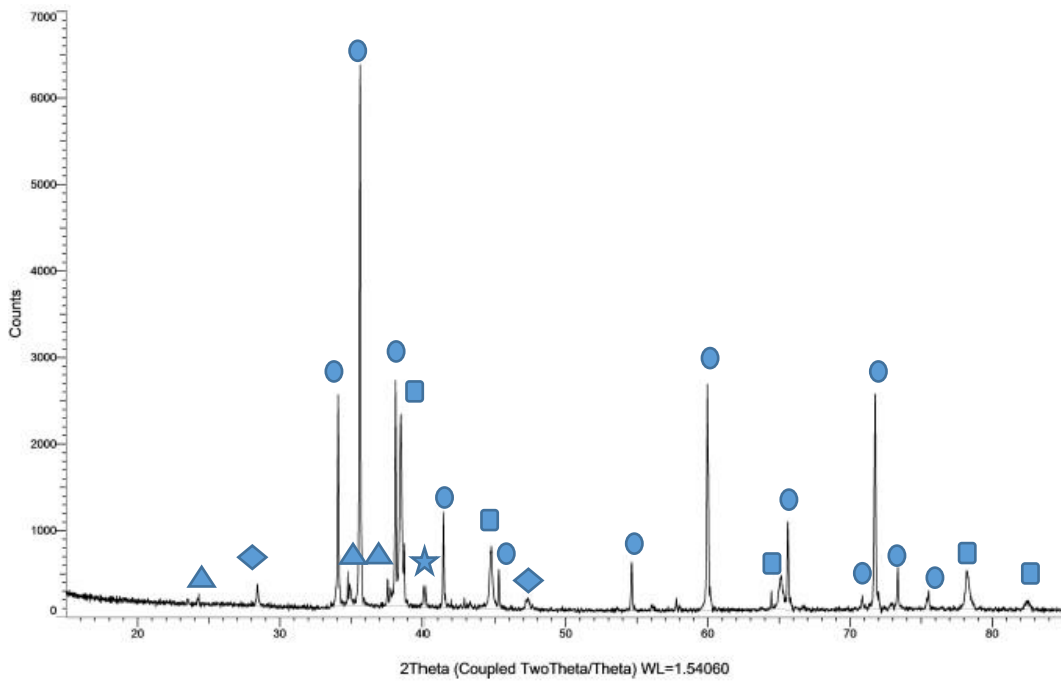


Figure 5.14. XRD analysis of Al alloy infiltrated 70S30B composite



**Figure 5.15.** XRD analysis of Al alloy infiltrated 80S20B composite



**Figure 5.16.** XRD analysis of Al alloy infiltrated 90S10B composite

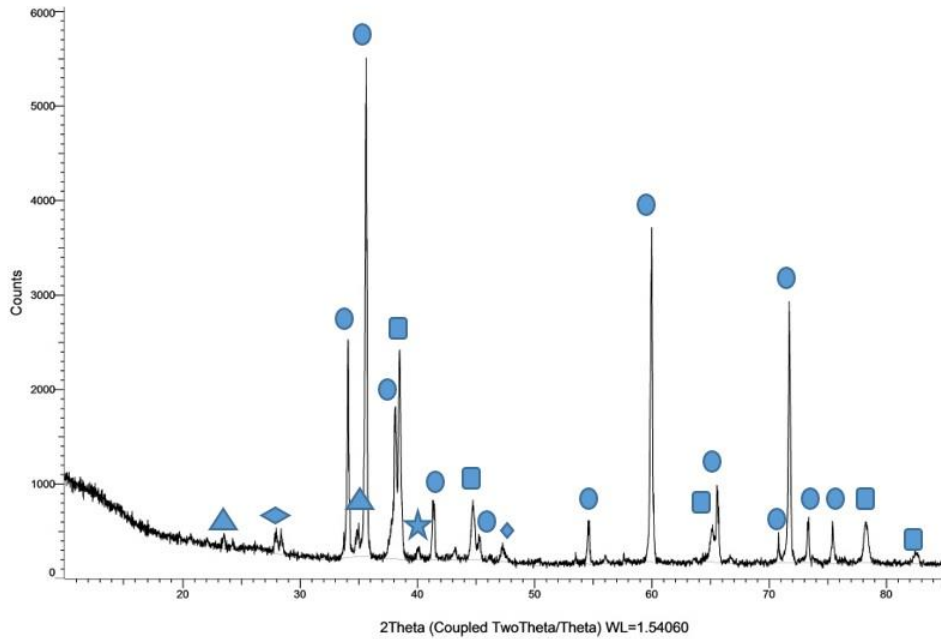


**Figure 5.17.** XRD analysis of Al alloy infiltrated FGM

## 5.6. OPTICAL MICROSCOPY ANALYSIS

Microstructural analysis and phase analysis were done with optical microscopy. But the images taken from optical microscopy were not clear due to lower magnification and resolution.

Figure 5.18 shows the microstructure of Al alloy which was infiltrated into ceramic preforms. The image was taken with 1000X magnification. Angular shape  $Mg_2Si$  phases distributed in the alloy matrix can be seen in Figure 5.18. These phases are brittle and cause decrease in percent elongation of the metal matrix alloy.

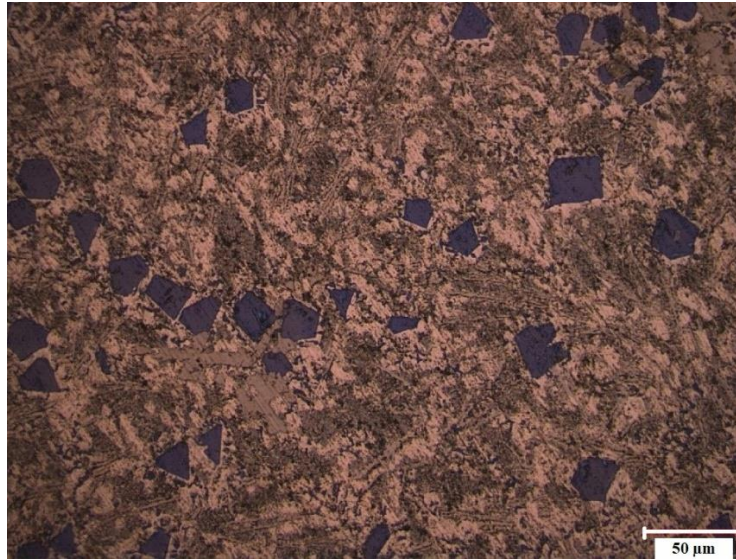


**Figure 5.18.** The microstructure of Al alloy

Al alloy infiltrated FGM was investigated with optical microscopy to detect gradually changing of microstructure. The image was taken with 50X magnification to obtain lower magnification so investigate all layers of FGM as illustrated in Figure 5.19. White and bright particles represent Al alloy. Since the highest porosity % is obtained for 90S10B, the vol. % of infiltrated Al alloy is the highest. Since the lowest porosity % is obtained for 70S30B, the vol. % of infiltrated Al alloy is the lowest. Thus, the vol. % of Al alloy decreases from 90S10B to 70S30B gradually with decreasing volume percent porosity. Microstructure shows inhomogeneous distribution of Al alloy. This may result from low ball milling time and hand-mixing of glucose-distilled water with powder compositions.

Phase analysis in terms of volume percent of infiltrated Al alloy was done to reveal variation in Al alloy infiltrated through section of FGM's layer as illustrated in Figure 5.20. The green areas represent Al alloy infiltrated. Phase analysis of FGM's layers which are (a) 90S10B, (b) 80S20B, (c) 70S30B as vol. % are given in Table 5.5. Vol. % of Al alloy decreases gradually from 90S10B layer to 70S30B layer.

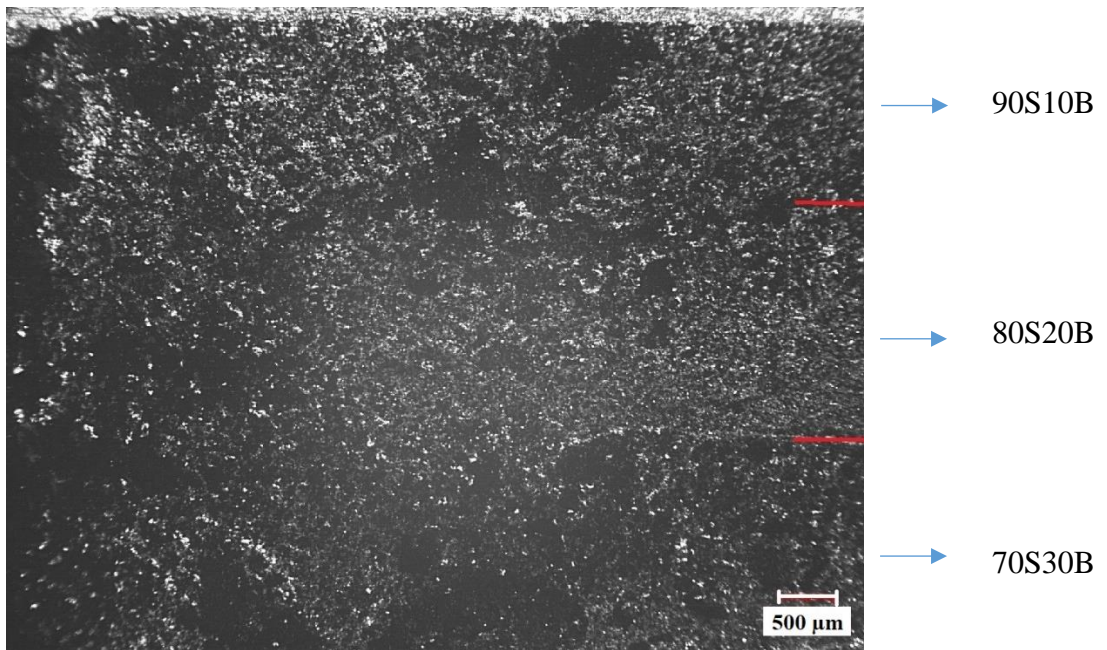


**Figure 5.19.** Microstructure of FGM

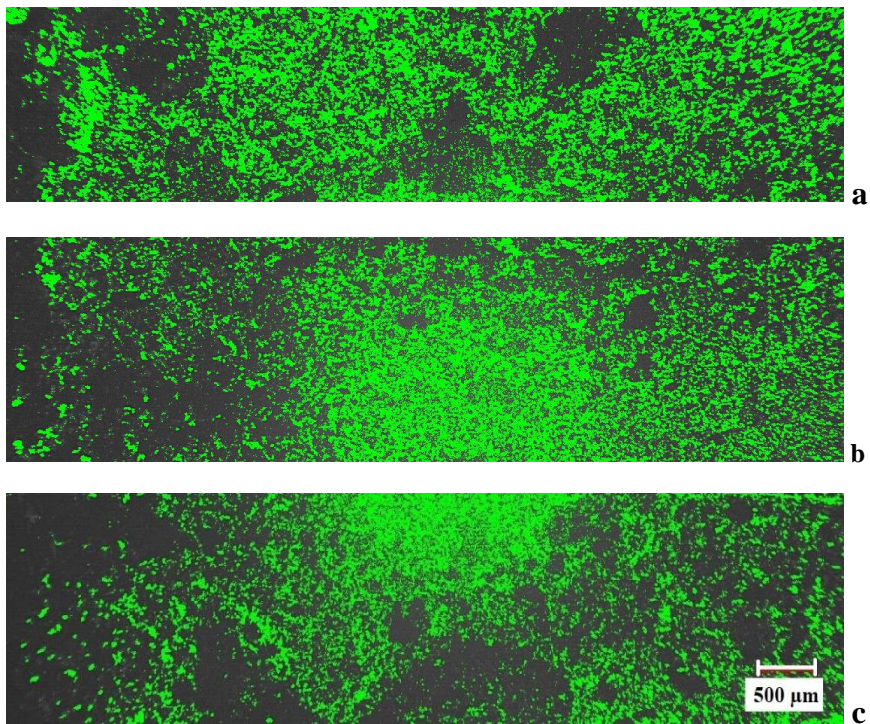


**Figure 5.20.** Phase analysis of FGM's layers which are (a) 90S10B, (b) 80S20B, (c) 70S30B

**Table 5.5.** Phase analysis of FGM's layers which are (a) 90S10B, (b) 80S20B, (c) 70S30B as vol. %

FGM's Layers	Black Area (vol. %)	Green Area (Al Alloy) (vol. %)
<b>90S10B</b>	66,6	33,4
<b>80S20B</b>	70,5	29,5
<b>70S30B</b>	77,4	22,6

Figure 5.21 shows each layer of Al alloy infiltrated FGM which are 90S10B, 80S20B and 70S30B and their vol. % of Al alloy. 5 images were taken with 100X magnification to do phase analysis. The white areas represent Al alloy infiltrated. The results were very close to the results represented in Table 5.5.

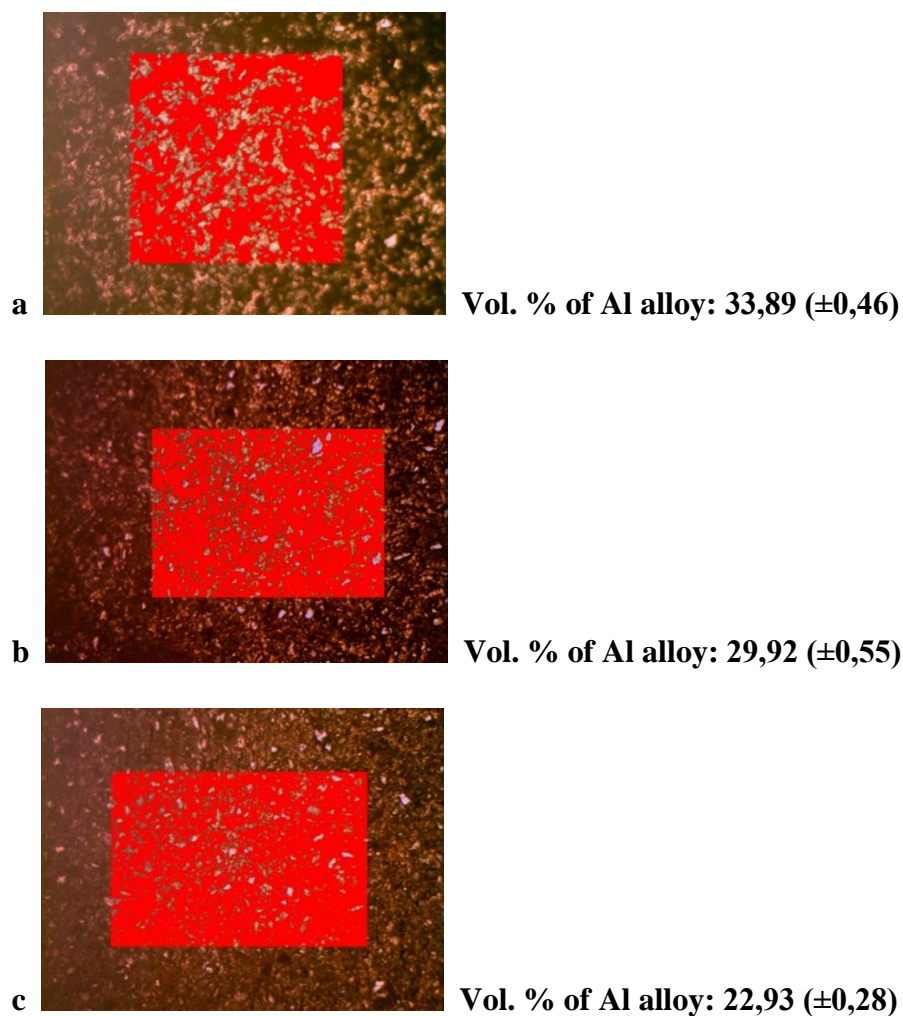


**Figure 5.21.** Phase analyses of Al alloy infiltrated (a) 90S10B, (b) 80S20B and (c)70S30B layers

## 5.7. SEM-EDX ANALYSIS

Microstructural analysis was done with scanning electron microscopy (SEM) and phase analysis was done with energy dispersive X-ray spectrometry (EDX). The images taken from SEM were clear due to higher magnification and resolution. The phases detected with XRD analysis can be confirmed by microstructure and peaks detected by SEM – EDX analysis.

Firstly, microstructure and particle size of B<sub>4</sub>C and SiC powders were examined by SEM analysis. B<sub>4</sub>C and SiC powders were embedded in epoxy resin separately, ground and polished prior to SEM analysis. Particle size and distribution results of B<sub>4</sub>C and SiC particles were confirmed that B<sub>4</sub>C has 1 μm particle size and SiC has 35 μm particle size with SEM analyses which are illustrated respectively in Figure 5.22 and Figure 5.23. Aspect ratios of B<sub>4</sub>C and SiC powders were also measured by dividing the long edge of the particle to short edge of the particle as shown in Table 5.6. The aspect ratio of B<sub>4</sub>C and SiC are very close to 1 which indicates the cubical or spherical shape.

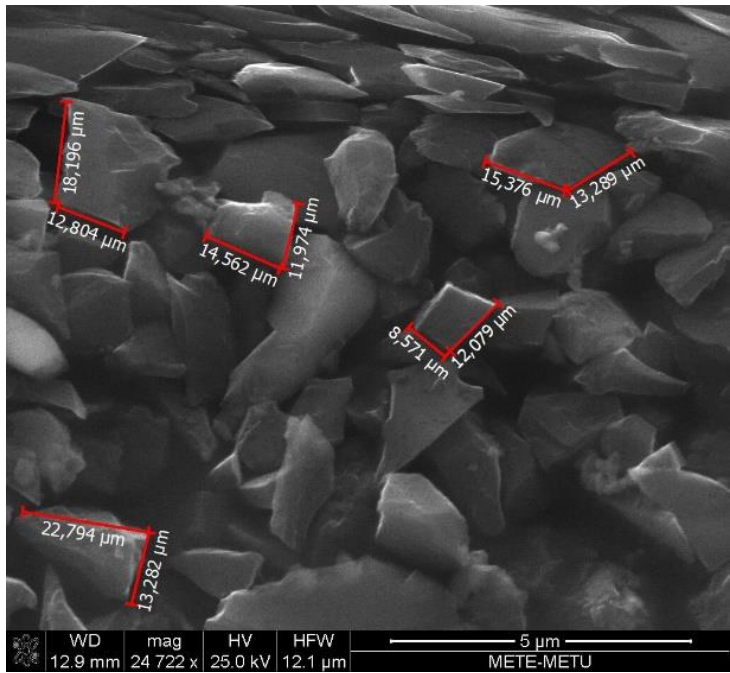


**Figure 5.22.** SEM analysis of B<sub>4</sub>C powder

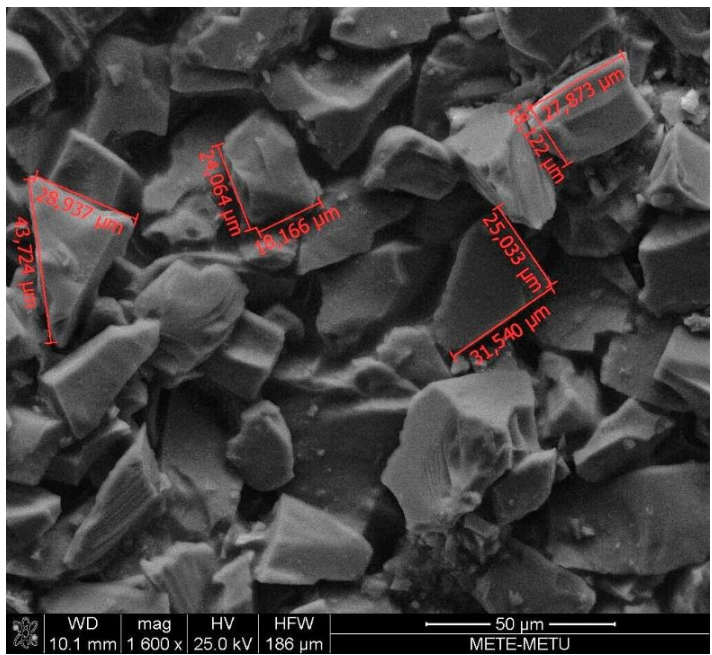


**Figure 5.23.** SEM analysis of SiC powder

**Table 5.6.** Aspect Ratio of B<sub>4</sub>C and SiC powders

<b>Powders</b>	<b>Aspect Ratio</b>
B <sub>4</sub> C	1,38 (±0,22)
SiC	1,41 (±0,14)

SEM-EDX analyses show that each layer of FGM and FGM were successfully infiltrated with Al alloy. It can be concluded that there is no difficulty in wetting of B<sub>4</sub>C – SiC ceramic by liquid aluminum alloy containing Mg and Si. Almost all the pores between ceramic particles were filled with Al alloy.

Bigger particles illustrated in Figure 5.24 with red circle represent SiC particles. Since the particle size of SiC is very large (35 μm) and the wt. % of SiC is more, SiC particles can be easily seen in the microstructure. This can be confirmed by EDX analysis as illustrated in Figure 5.24. EDX analysis was applied to this particle and it revealed only Si and C peaks that confirmed this particle is SiC. This image was taken from Al alloy infiltrated 80S20B composite. The particle size of SiC was also confirmed by the magnification bar at right below the image.

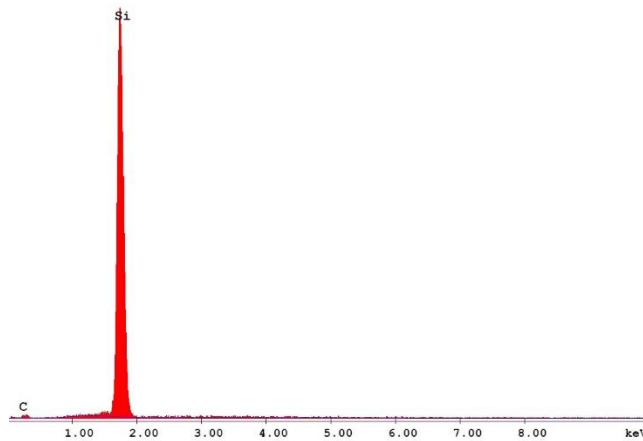
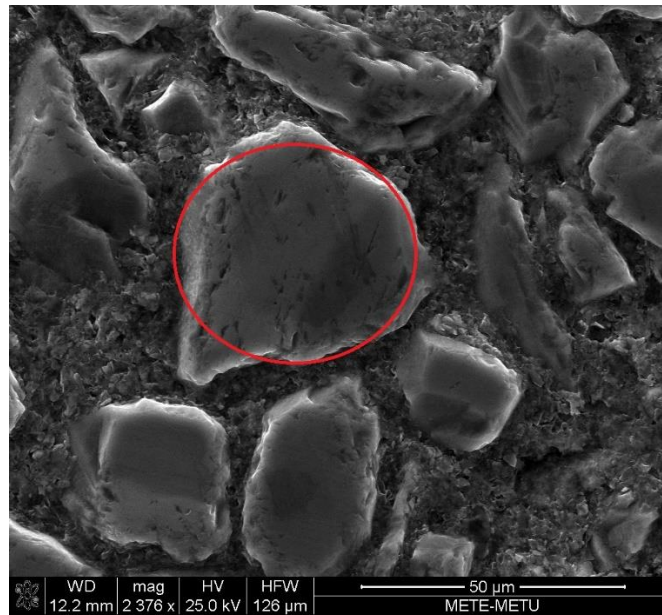


**Figure 5.24.** SEM-EDX analysis of SiC region of Al infiltrated 80S20B composite

Figure 5.25 shows the SEM image of the Al alloy region of infiltrated 80S20B composite. This can be confirmed by EDX analysis as illustrated in Figure 5.25. EDX analysis was applied to this region and it revealed only Al, Mg, Zn, Cu and Si peaks that are ingredients of infiltrated Al alloy. Figure 5.25 also shows the SEM image of the B<sub>4</sub>C region of Al alloy infiltrated 80S20B composite. Small black particles in the Al alloy represent B<sub>4</sub>C particles as illustrated in Figure 5.25 and it can be seen at higher magnification such as 7416X. Since the particle size of B<sub>4</sub>C is very small and the wt.

% of B<sub>4</sub>C is low, B<sub>4</sub>C particles can be hardly seen in the microstructure. This could not be confirmed by EDX analysis because boron and carbon elements could not be detected correctly with this analysis due to, they are light elements.

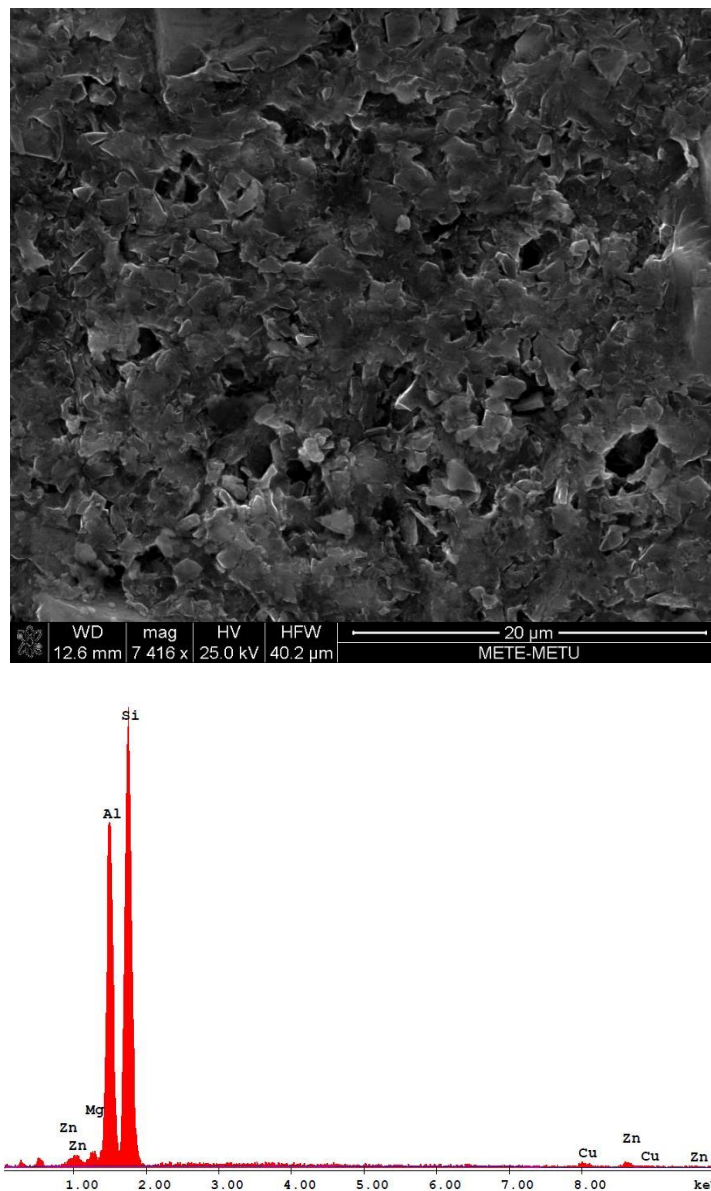


**Figure 5.25.** SEM-EDX analysis of Al alloy / B<sub>4</sub>C region of Al alloy infiltrated 80S20B composite

Figure 5.26 shows  $Mg_2Si$  phase as the angular shape which was drawn with red lines detected at Al alloy infiltrated 80S20B composite. This phase is embedded in Al alloy and it can be seen at higher magnification such as 13000X. By EDX analysis Mg and Si elements in  $Mg_2Si$  and Al element around  $Mg_2Si$  were detected. Although these elements dissolved at the time of infiltration,  $Mg_2Si$  formed again at the time of solidification.  $Mg_2Si$  phase was also detected by XRD analyses and confirmed by SEM-EDX analysis.

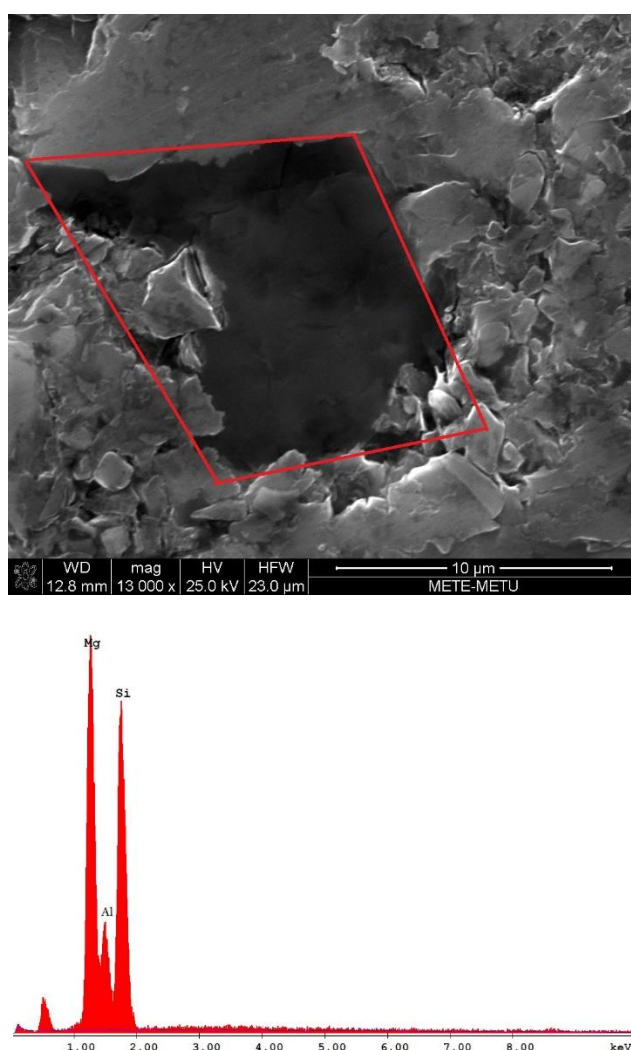


**Figure 5.26.** SEM-EDX analysis of  $Mg_2Si$  region of Al alloy infiltrated 80S20B composite

## 5.8. HARDNESS MEASUREMENTS

Hardness were measured on Al alloy infiltrated 90S10B, 80S20B and 70S30B composites whose results are given in Table 5.7. Hardness measurements were done 5 times in the HRC scale by using 150 kg load. Then results were averaged. Since they are ceramic-metal composite, hardness of aluminum and ceramic rich regions revealed low and high values. Therefore, standard deviations are high among each layer and datas were scattered. But the average hardness values of each layer is close to each other. However, 70S30B layer has the highest hardness value and this layer can be considered as a front layer that breaks up to projectile into small pieces due to its highest hardness value if this composite is to be used for ballistic application. 70S30B layer contains the highest wt. % B<sub>4</sub>C having higher hardness value than the hardness of SiC and the lowest vol. % Al phase which increases the hardness value due to increase in volume fraction of ceramic phases.

**Table 5.7.** Hardness measurements of Al alloy infiltrated 90S10B, 80S20B and 70S30B composites

<b>Layer</b>	<b>Hardness (HRC)</b>
90S10B	36,96 (± 3,53)
80S20B	33,14 (± 2,05)
70S30B	38,82 (± 2,24)

## 5.9. THREE POINT BEND TEST

Three point bend tests were done to Al alloy and Al alloy infiltrated 90S10B, 80S20B and 70S30B composites whose results are given in Table 5.8. Al alloy exhibits the highest flexural strength. In terms of Al alloy infiltrated 90S10B, 80S20B and 70S30B composites, because 90S10B layer includes less wt. % B<sub>4</sub>C and more vol. % Al alloy

due to its highest porosity %, flexural strength is the highest for 90S10B layer. Since 70S30B layer includes more wt. % B<sub>4</sub>C and less vol. % Al alloy due to its lowest porosity %, flexural strength is the lowest for 70S30B layer. Flexural strength decreases gradually as illustrated in Figure 5.27. 90S10B layer may be considered as a backing layer that absorbs the remaining kinetic energy of propellants due to its highest flexural strength if this composite is to be used for ballistic application. Flexure load versus flexure extension graphs are illustrated in Appendix.

**Table 5.8.** Three point bend test results

	<b>Flexural Strength (MPa)</b>
<b>Al Alloy</b>	280 (± 17)
<b>90S10B</b>	193 (± 12)
<b>80S20B</b>	131 (± 1)
<b>70S30B</b>	111 (± 3)

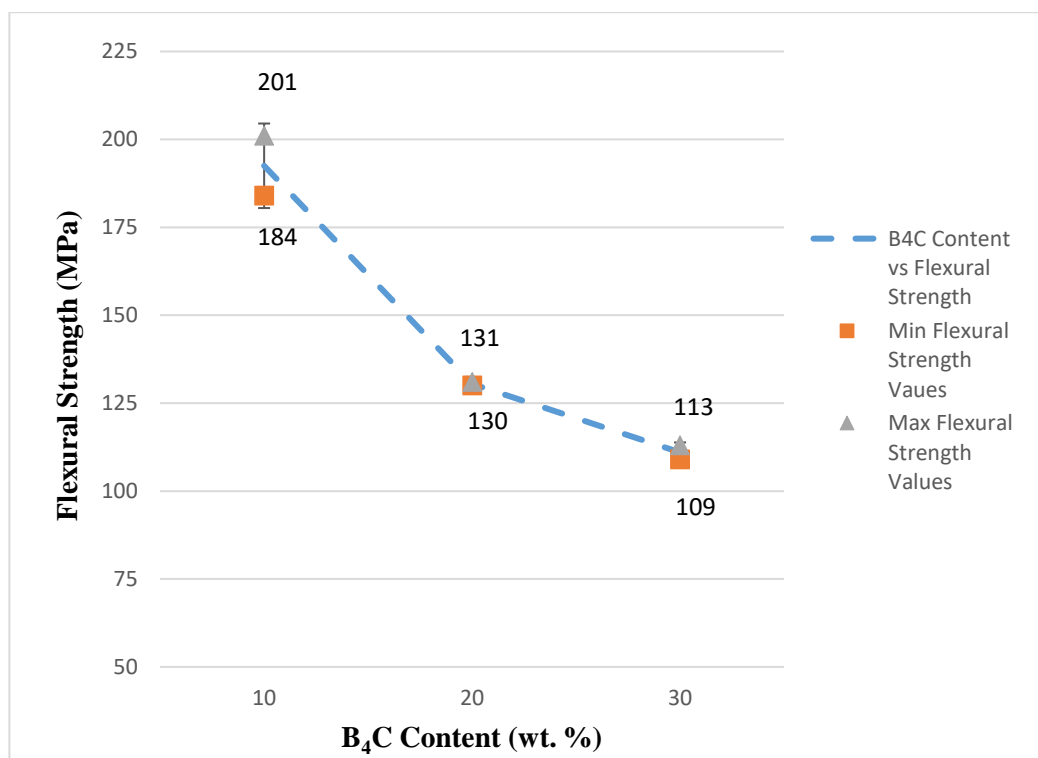


**Figure 5.27.** Flexural strength with respect to B<sub>4</sub>C content

Three point bend tests were done FGM. 1 cm height ceramic-metal composites which consist of 3 different layers of FGM (90S10B, 80S20B and 70S30B) with 1,3 cm height Al alloy base were tested. Compression was applied from the ceramic-metal composite part (70S30B layer) which was developed for the front layer that projectile strikes. Flexure load versus flexure extension graphs are illustrated in Appendix and flexural strength was found 348 ( $\pm 40$ ) MPa . M. V. Silva et. al. [28] was applied three point bend test to 1 cm height sintered alumina plates and the results were 210 to 300 MPa. These alumina based ballistic plates (0,3 cm polyurethane + 1,2 cm sintered alumina + 0,4 cm SAE 1045 Steel) were also exposed to ballistic tests according to NIJ Level IV threat type and none of the plates were penetrated. This result shows that FGM can be considered as a potential candidate for armor material because the flexural strength of FGM is higher than the values reported in the literature.

Figure 5.28 shows FGM specimen subjected to three point bend test.

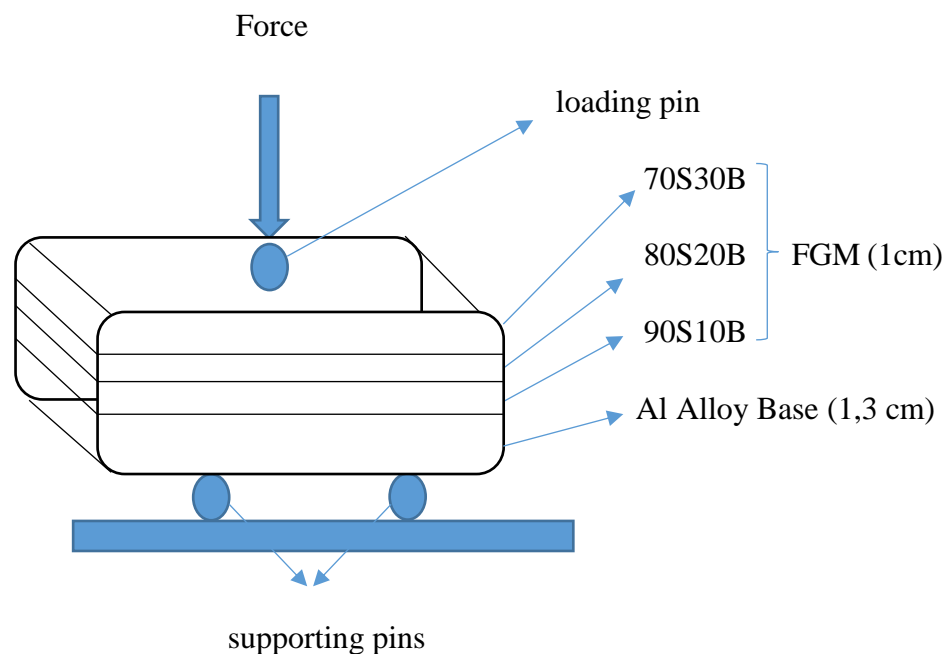


**Figure 5.28.** FGM with Al alloy base specimen subjected to three point bend test



## CHAPTER 6

### CONCLUSIONS

#### 6.1. CONCLUSIONS

The major conclusions drawn from the results of experiments as follows:

- B<sub>4</sub>C – SiC – Al composite which has low density ( $2,7 \pm 0,02 \text{ g/cm}^3$ ) and a combination of high hardness (up to  $38,82 \pm 2,24 \text{ HRC}$ ) and high flexural strength ( $348 \pm 40 \text{ MPa}$ ) was produced by pressure melt infiltration process to obtain FGM.
- Composition is the most important variable to obtain gradual changing bulk density and porosity which are the requirements of an FGM sample. To develop FGM, three different layers (90S10B - 80S20B - 70S30B) with different bulk densities ( $2,06 \pm 0,03 - 2,14 \pm 0,02 - 2,28 \pm 0,03 \text{ g/cm}^3$ ) and different porosity % ( $34,2 \pm 0,91 - 29,6 \pm 1,21 - 23,2 \pm 0,88$ ) was produced by altering composition respectively.
- Since the highest porosity % is obtained for 90S10B, the vol. % of infiltrated Al alloy is the highest. Since the lowest porosity % is obtained for 70S30B, the vol. % of infiltrated Al alloy is the lowest. Thus, the vol. % of Al alloy decreases from 90S10B to 70S30B gradually with respect to porosity % results.

- FGM produced exhibits gradually increment of flexural strength ( $111 \pm 3 - 131 \pm 1 - 193 \pm 12 - 280 \pm 17$  MPa) for 70S30B, 80S20B, 90S10B and Al alloy respectively which make it a potential candidate for armor applications.
- Flexural strength for FGM  $B_4C$ -SiC-Al with dimensions of 12 cm length, 4 cm width and 2,3 cm thickness (1 cm height ceramic-metal composite with 90S10B, 80S20B and 70S30B layers and 1,3 cm height Al alloy base) was found  $348 \pm 40$  MPa. This result shows that FGM can be considered as a potential candidate for armor material because this value is higher than the values (210 – 300 MPa) reported in the literature.
- The new composition of Al alloy which had 11,2 wt. % Si and 6,9 wt. % Mg for pressure melt infiltration process was modified from 7075 Al alloy. Microstructure investigation showed that this composition was suitable to achieve process and to produce an almost pore-free composite.
- Near or near-net shape products were produced as mass production with this pressure melt infiltration process.
- With pressure melt infiltration, the sintered body was exposed to Al metal only a few seconds. Thus, there was no time to react Al element with carbide to yield detrimental  $Al_4C_3$  phase together with  $B_4C$  and SiC particles. Elimination of this detrimental phase increased mechanical performance of composites developed.

## 6.2. RECOMMENDATIONS FOR FUTURE STUDY

- For future study, FGM may be exposed to the ballistic tests and modified according to results. To do that a bigger specimen dimensions suitable for ballistic tests should be studied. Figure 6.1 illustrates the armor design for future study. Fabric cover to protect ballistic plate from weathering conditions and to provide integrity of the materials inside the ballistic plate can be used. And some polymer backing such as aramid, UHMWPE, glass fiber, carbon fiber may be considered in addition to ceramic-metal composite.

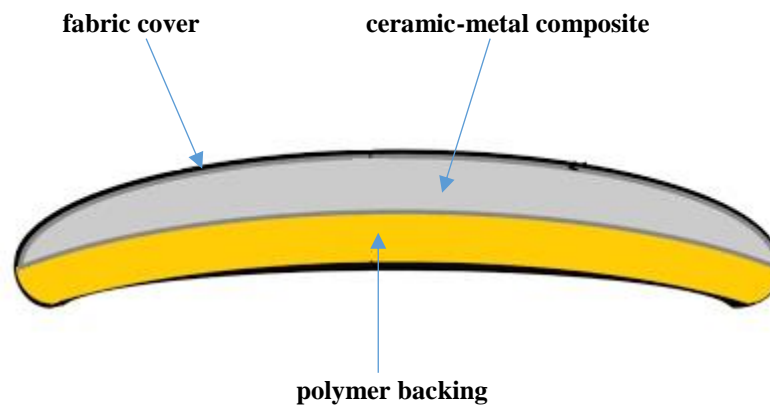


**Figure 6.1.** Armor design for future study

- Since sintered ceramic exhibits high hardness, there is a machining problem. When the same mold is used for both pressing of powders and pressure melt infiltration, sintered ceramic does not fit mold due to thermal expansion. Thus, it is recommended that a mold used for pressure melt infiltration should be larger than a mold used for the pressing of powders to obtain green body.



## REFERENCES

- [1] M. Übeyli, E. Balcı, B. Sarıkan, M. K. Öztaş, N. Camuşcu, R. O. Yıldırım and Ö. Keleş, The ballistic performance of SiC-AA7075 functionally graded composite produced by powder metallurgy, *Materials and Design* 56:31-36, April 2014.
- [2] C. S. Lee, X. F. Zhang, G. Thomas, Novel joining of dissimilar ceramics in the Si<sub>3</sub>N<sub>4</sub>-Al<sub>2</sub>O<sub>3</sub> system using polytypoid functional gradients, *Acta Materialia* 49(18):3775-3780, October 2001.
- [3] D. B. Rahbek and B. B. Johnsen, Dynamic behaviour of ceramic armour systems, FFI-rapport 2015/01485, Norwegian Defence Research Establishment (FFI), November 2015.
- [4] S. K. Bohidar, R. Sharma, P. R. Mishra, Functionally Graded Materials: A Critical Review, *International Journal of Research (IJR)* Vol-1, Issue-7, August 2014.
- [5] J. Yu, A. Kidane, Modeling functionally graded materials containing multiple heterogeneities, *Acta Mechanica* 225(7):1931–1943, July 2013.
- [6] M.P. Dariel, L. Levin, N. Frage, Graded ceramic preforms: various processing approaches, *Materials Chemistry and Physics* 67(1-3):192-198, January 2001.
- [7] M. Koizumi, FGM activities in Japan, *Composites Part B:Engineering* 28(1-2):1-4, 1997.

[8] P. G. Karandikar, G. Evans, S. Wong, M. K. Aghajanian, M. Sennett, A review of ceramics for armor applications, In: Advances in Ceramic Armor IV, Ceramic Engineering and Science Proceedings, Volume 29, Issue 6, pp. 163-175, April 2009.

[9] National Institute of Justice, Ballistic Resistance of Personal Body Armor NIJ Standard-0101.04, September 2000

[10] G. Arslan, Bor Karbür-Alüminyum Kompozitlerin Üretimi ve Karakterizasyonu, Doktora Tezi, Anadolu Üniversitesi Seramik Mühendisliği Bölümü, 2001.

[11] X. Yue, J. Wang, X. Li, L. You, H. Ru, Microstructures and mechanical properties of a two-layer  $B_4C/Al-B_4C/TiB_2$  composite, Materials Science and Engineering A 559:719-724, January 2013.

[12] M. M. Balakrishnarajan, P. Pancharatna, R. Hoffmann, Structure and bonding in boron carbide: The invincibility of imperfections, New Journal of Chemistry 31(4), April 2007.

[13] G. Arslan, F. Kara, S. Turan, Quantitative X-ray diffraction analysis of reactive infiltrated boron carbide-aluminium composites, Journal of the European Ceramic Society 23(8):1243-1255, July 2003.

[14] C. Roberson P. J. Hazell, Resistance of Silicon Carbide To Penetration By A Tungsten Carbide Cored Projectile, Advanced Defence Materials Ltd. and Cranfield University in U.K.

[15] G. Arslan, A. Kalemtaş, Processing of silicon carbide-boron carbide-aluminium composites, Journal of the European Ceramic Society 29: 473-480, March 2009.

- [16] A. Kalkanlı, T. Durmaz, A. Kalemtaş, G.Arslan, Melt Infiltration Casting of Alumina Silicon Carbide and Boron Carbide Reinforced Aluminum Matrix Composites, Journal of Materials Sciences & Engineering, January 2017.
- [17] I. Gunjishima, T. Akashi, T. Goto, Characterisation of Directionally Solidified B<sub>4</sub>C-SiC Composites Prepared by a Floating Zone Method, Materials Transactions 43(4):712-720, September 2002.
- [18] H. Nanda, G. J. Appleby-Thomas, D. Wood, P. Hazell, Ballistic behaviour of explosively shattered alumina and silicon carbide targets, Advances in Applied Ceramics 110(5):287-292, July 2011.
- [19] M. Mashhadi, E. Taheri-Nassaj, V. M. Sglavo, H. Sarpoolaky, N. Ehsani, Effect of Al addition on pressureless sintering of B<sub>4</sub>C, Ceramics International 35(2):831–837, 2009.
- [20] A. Kalemtaş, Production of Some Non-Oxide Ceramic-Aluminum Composites via Pressureless Infiltration Technique, Department of Metallurgical and Materials Engineering / Bursa Technical University, January 2016.
- [21] İ. Bilici, M. Gürü, S. Tekeli, Production of Ti-Fe Based MgAl<sub>2</sub>O<sub>4</sub> Composite Material by Pressureless Infiltration Method, Gazi University Journal of Science, 28(2):295-299, July 2015.
- [22] Halverson, Boron-Carbide-Aluminum And Boron Carbide Reactive Cermets, United States Patent, Patent Number: 4,605,440, Date of Patent: Aug. 12, 1986.

[23] A. M. Zahedi, H. R. Rezaie, J. Javadpour, M. Mazaheri, M. G. Haghighi, Processing and impact behavior of Al/SiC<sub>p</sub> composites fabricated by the pressureless melt infiltration method, *Ceramics International* 35:1919-1926, 2009.

[24] N. Tuncer, B. Tasdelen, G. Arslan, Effect of passivation and precipitation hardening on processing and mechanical properties of B<sub>4</sub>C–Al composites, *Ceramics International* 37(7): 2861–2867, September 2011.

[25] Pyzik, Light Weight Boron Carbide/Aluminum Cermets, United States Patent, Patent Number: 5521016, Date of Patent: May 28, 1996.

[26] M. Chedru, J. Vicens, J. L. Chermant, B. L. Mordike, Aluminium–aluminium nitride composites fabricated by melt infiltration under pressure, *Journal of Microscopy* 196(Pt 2):103-112, December 1999.

[27] H. S. Lee, S. H. Hong, Pressure infiltration casting process and thermophysical properties of high volume fraction SiC<sub>p</sub> / Al metal matrix composites, *Materials Science and Technology* 19(8):1057-1064, August 2003.

[28] M. V. Silva, D. Stainer, H. A. Al-Qureshi, O. R. K. Montedo and D. Hotza, Alumina-based ceramics for armor application: mechanical characterization and ballistic testing, *Journal of Ceramics* Volume 2014, Article ID 618154, 9 January 2014.

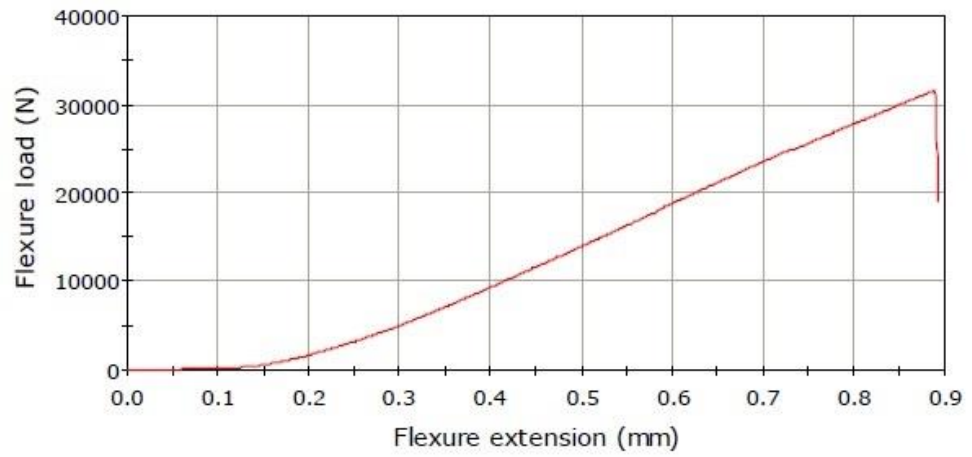
[29] G. Arslan, Bor Karbür – Alüminyum Kompozitlerinin Üretimi ve Karakterizasyonu, Doktora Tezi, Fen Bilimleri Enstitüsü, Seramik Mühendisliği Anabilim Dalı, Mart 2001.

[30] T. Williams, Development of Pressureless Sintered Silicon Carbide – Boron Carbide Composites for Armor Applications, Thesis Submission, Engineering Doctorate (Micro and Nano Materials), 2015.

[31] C. Christos, Analysis of the three-point-bend test for materials with unequal tension and compression properties, NASA Technical Note (NASA TN D-7572), Lewis Research Center Cleveland Ohio 44135.



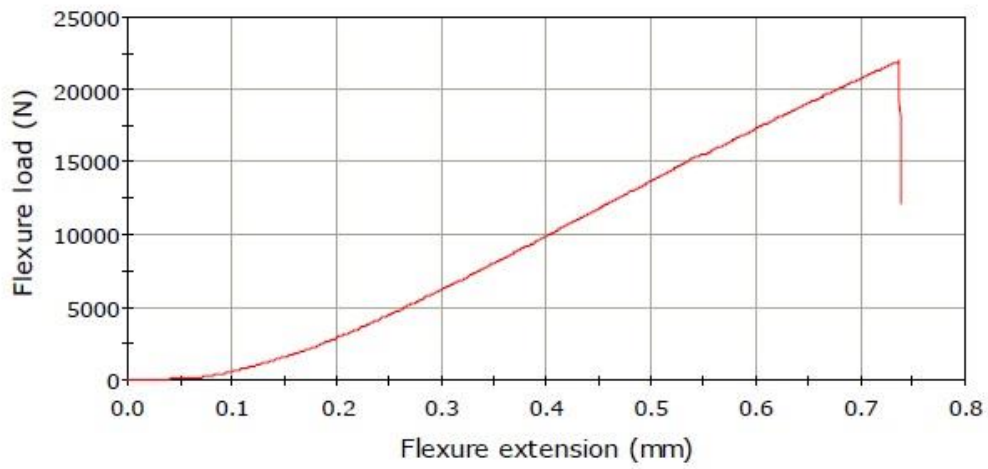
## APPENDIX



$$c = h/2$$
$$h = 18 \text{ mm}$$

	Flexure load at Maximum Flexure stress (N)	Maximum Flexure stress (MPa)
1	31577.74414	292.13495

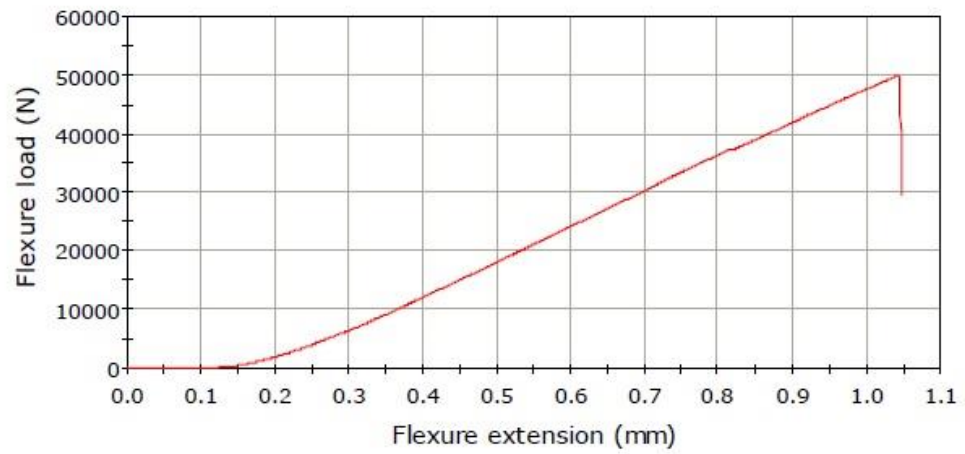
Figure A. 1. Flexure load-Flexure extension graph of Al alloy specimen 1



**$c = h/2$**   
 **$h = 15.7 \text{ mm}$**

	Flexure load at Maximum Flexure stress (N)	Maximum Flexure stress (MPa)
1	21971.73633	266.98361

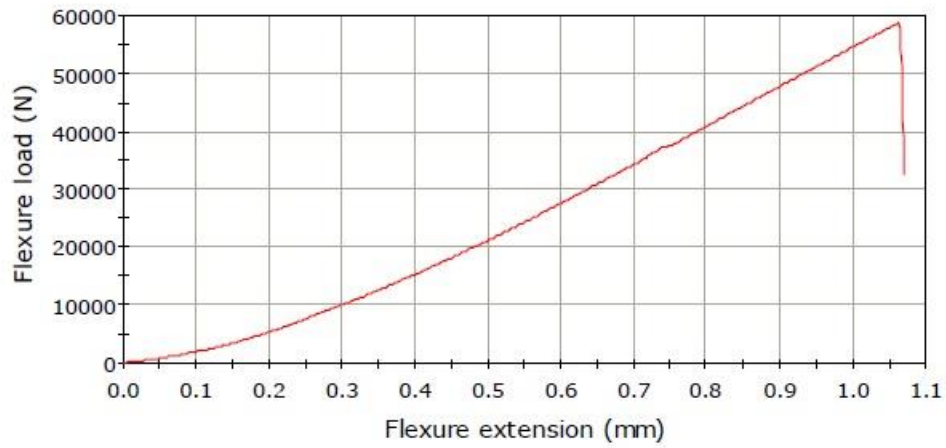
**Figure A. 2.** Flexure load-Flexure extension graph of Al alloy specimen 2



**$c = 0.565h$**   
 **$h = 23 \text{ mm}$**

	Flexure load at Maximum Flexure stress (N)	Maximum Flexure stress (MPa)
1	50001.99609	283.56213

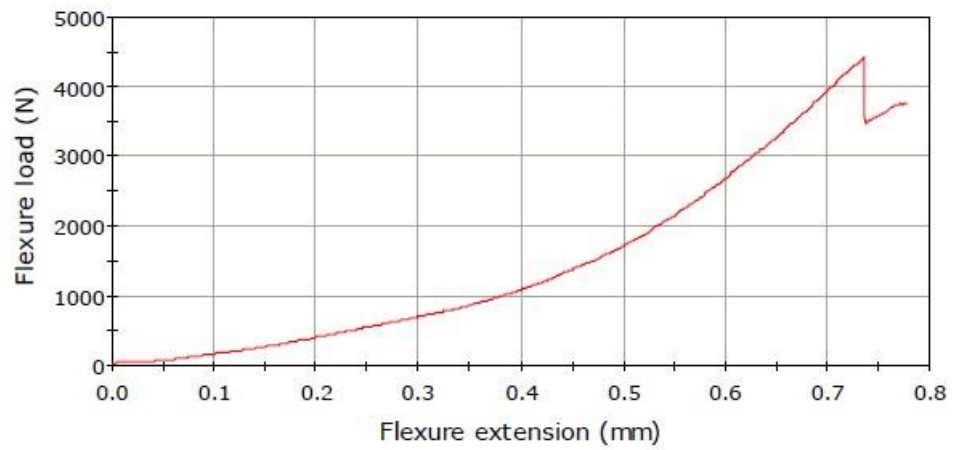
**Figure A. 3.** Flexure load-Flexure extension graph of FGM specimen 1



**$c = 0.565h$**   
 **$h = 23 \text{ mm}$**

	Flexure load at Maximum Flexure stress (N)	Maximum Flexure stress (MPa)
1	58738.65625	330.40494

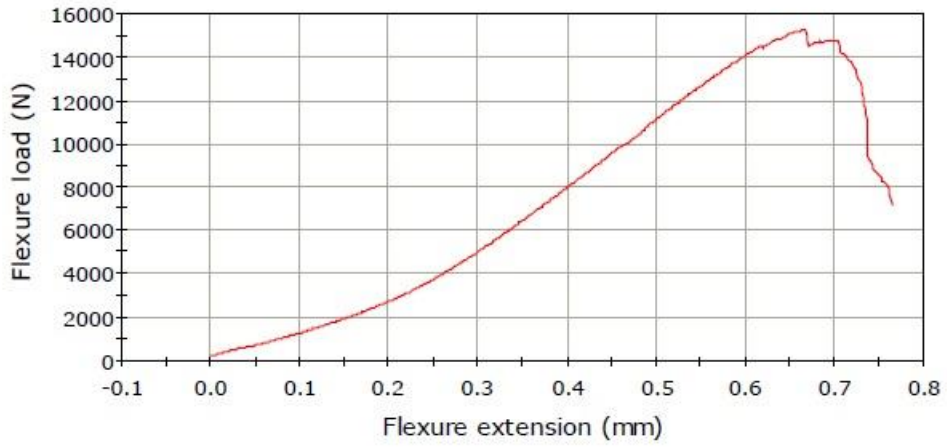
**Figure A. 4.** Flexure load-Flexure extension graph of FGM specimen 2



**$c = h/2$**   
 **$h = 11 \text{ mm}$**

	Flexure load at Maximum Flexure stress (N)
1	4412.75146

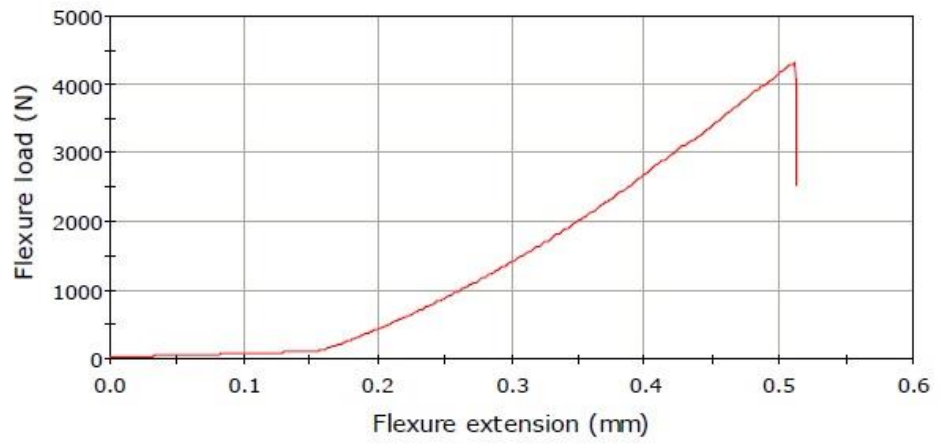
**Figure A. 5.** Flexure load-Flexure extension graph of Al alloy infiltrated 70S30B specimen 1



**$c = h/2$**   
 **$h = 20.1 \text{ mm}$**

	Flexure load at Maximum Flexure stress (N)	Maximum Flexure stress (MPa)
1	15261.54590	108.19294

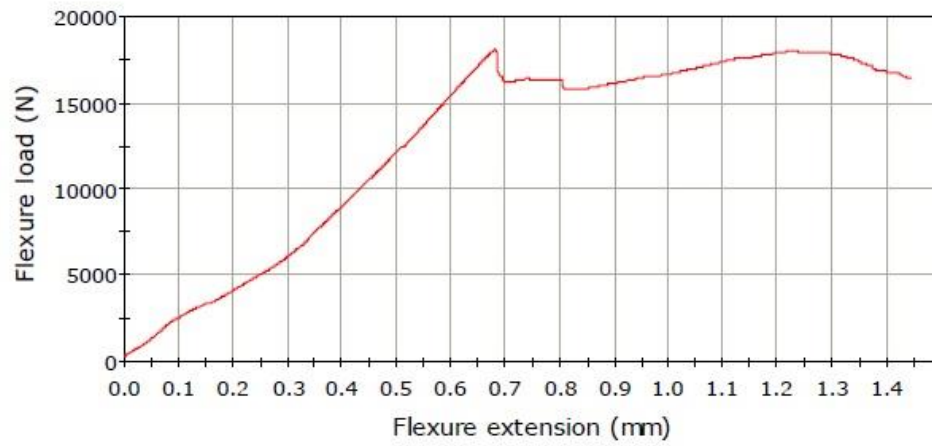
**Figure A. 6.** Flexure load-Flexure extension graph of Al alloy infiltrated 70S30B specimen 2



**$c = h/2$**   
 **$h = 10 \text{ mm}$**

	Flexure load at Maximum Flexure stress (N)
1	4320.51904

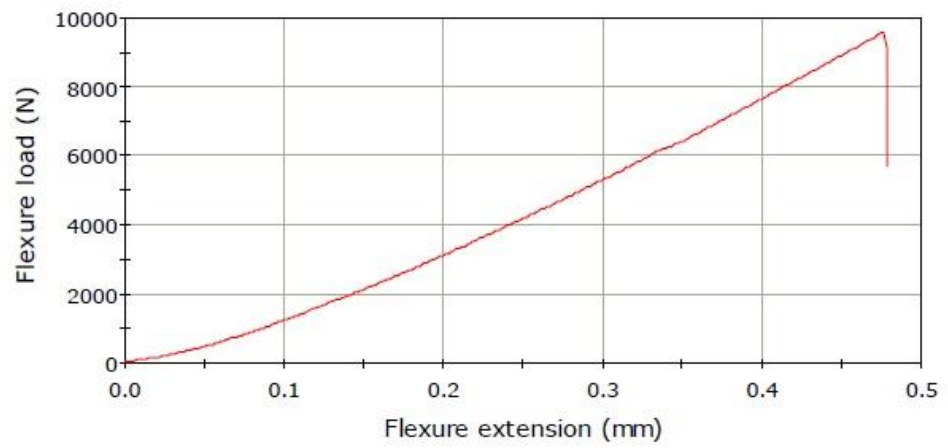
**Figure A. 7.** Flexure load-Flexure extension graph of Al alloy infiltrated 80S20B specimen 1



**$c = h/2$**   
 **$h = 20.4 \text{ mm}$**

	Flexure load at Maximum Flexure stress (N)	Maximum Flexure stress (MPa)
1	18158.55078	127.14342

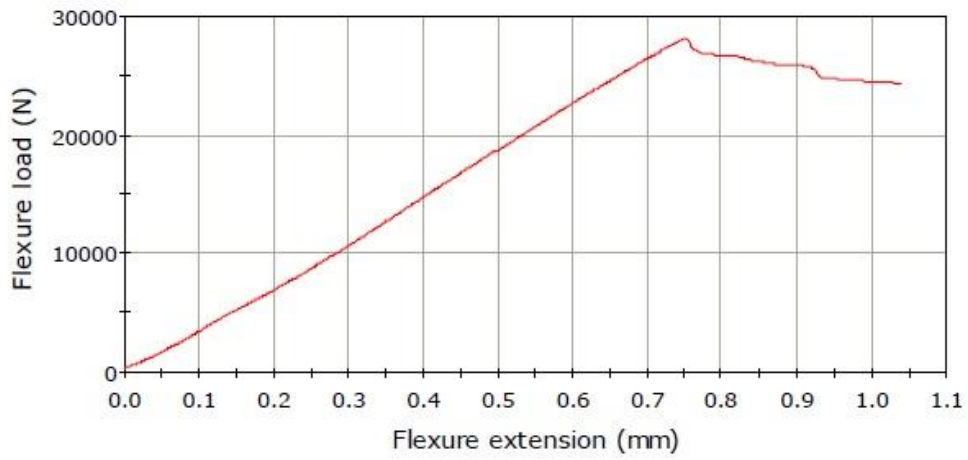
**Figure A. 8.** Flexure load-Flexure extension graph of Al alloy infiltrated 80S20B specimen 2



**$c = h/2$**   
 **$h = 12.5 \text{ mm}$**

	Flexure load at Maximum Flexure stress (N)
1	9600.15137

**Figure A. 9.** Flexure load-Flexure extension graph of Al alloy infiltrated 90S10B specimen 1



**$c = h/2$**   
 **$h = 20.5 \text{ mm}$**

	Flexure load at Maximum Flexure stress (N)	Maximum Flexure stress (MPa)
1	28120.45508	187.23705

**Figure A. 10.** Flexure load-Flexure extension graph of Al alloy infiltrated 90S10B specimen 2